Design and Testing of a 1.5 m Offset CRTS Demonstrator

C.Y. Lai and S. Pellegrino

CUED/D-STRUCT/TR193

European Space Agency Contractor Report

The work presented in this report was carried out under an ESA contract.

Responsibility for its contents resides with the authors.

ESA Study Manager: W.J. Rits

ESTEC Contract no. 11936/96/NL/FG

Release date: 20 March 2001

Abstract

This report presents the design, construction and testing of a 1.5 m diameter Collapsible Rib-Tensioned Surface (CRTS) reflector demonstrator with offset configuration, based on the circular configuration introduced in a previous report in this series. Key features of the design are: simplicity; ease of assembly, dismantling and adjustment; hub size capable of smooth and controlled expansion; and surface accuracy controlled by the membrane, not by the ribs. The root-mean-square surface error of the demonstrator is found to be 2.0 mm, practically coinciding with the value that had been predicted analytically. The demonstrator has been packaged by wrapping the membrane and ribs around the hub. Deployment takes about 1 s, and the deployment sequence has been found to be very repeatable.

Contents

List of Figures

List of Tables

Chapter 1

Introduction

This report presents the design, construction and testing of a 1.5 m diameter Collapsible Rib-Tensioned Surface (CRTS) reflector model with offset configuration. Of the three different offset configurations introduced in Lai and Pellegrino (1999), the circular configuration was chosen because it allows a more uniform prestress distribution in the reflector surface. Figure 1.1 shows a schematic front view.

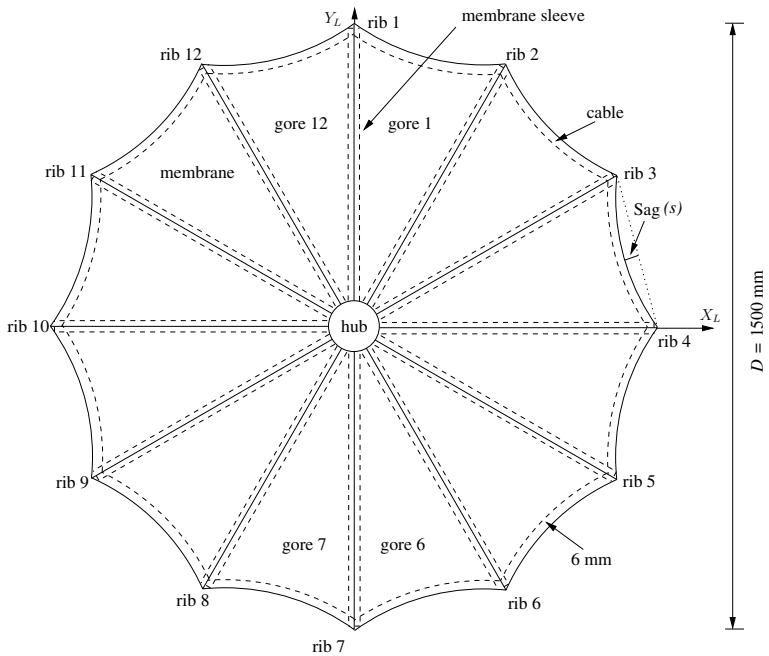

Figure 1.1: Schematic top view of the offset reflector model.

The whole structure is supported by a central expandable hub and the membrane surface is supported by twelve ribs radially connected to the hub. A cable is connected to the outer edge of the membrane surface and passes through the tip of each rib, starting and ending at rib 1. The numbering of the ribs is also shown.

The number of ribs used in the reflector is dependent on the required surface accuracy, see Table 7.1 in Lai and Pellegrino (1999). Of course, higher surface accuracies are achieved by using a larger number of ribs; however, the cost, mass, and complexity of the reflector and most importantly its packaged size also increase. In the present case there were no specific requirements, but it was decided to aim for the highest possible accuracy that could be achieved within the budget of the present project, hence twelve ribs were chosen.

1.1 Objectives

The key objective of the present study was to develop and demonstrate a design process for offset CRTS reflectors. Particular emphasis was placed on the following.

- Simplicity, to reduce the manufacturing complexity and cost, and to increase reliability and accuracy.
- Ease of assembly, dismantling and adjustment.
- Hub size to be small as possible to minimise the packaged size.
- Hub expansion to be smooth and controlled, with the possibility of adjustment to modify the prestress of the membrane.
- Reflector accuracy to be controlled by the membrane, not by the ribs.

1.2 Design Approach

The following important decisions were taken right at the beginning of the design process.

It was decided that the reflecting membrane surface would be formed by a series of *flat* pieces, or gores joined along their edges. In future, it may well be possible to manufacture the gores from curved foils, but this was not a practical option at this stage. The only Kevlar-reinforced Kapton foil that could be made available for this project was flat. The possibility of using unreinforced Kapton foil was considered, because its lower elastic modulus would allow it to stretch into a doubly-curved surface. However, the CRTS reflector concept envisages the membrane being in-plane stiff, and hence it was decided to use the stiffer material.

Since it had been previously shown that biaxial prestress distributions in CRTS reflectors made from flat gores are very poor, see Figure 3.8 of Lai, You and Pellegrino (1997), it was decided to aim for an essentially uniaxial prestress of the membrane surface, in the hoop direction. An advantage of taking this line is that it becomes possible, at least theoretically, to design CRTS reflectors

that follow the shape of the *reference surface*[1]; Section 3.3 of Lai and Pellegrino (1999) shows how to set up such a stress distribution in an offset reflector. For the particular case of a *circular offset reflector*, see Section 2.4 of Lai and Pellegrino (1999), the prestress is a uniform hoop stress.

In the present study the stresses in the membrane will not be measured by strain gauges and hence the stress level can be much smaller than in the preliminary tests carried out by Lai, You and Pellegrino (1997). The membrane prestress needs to be sufficiently large to practically remove all creases formed during packaging and to provide sufficient geometric stiffness to the membrane that very low frequency vibration modes are avoided, see Kukathasan and Pellegrino (2001). In conclusion, the prestress distribution that is aimed for is shown in Fig. 1.2.

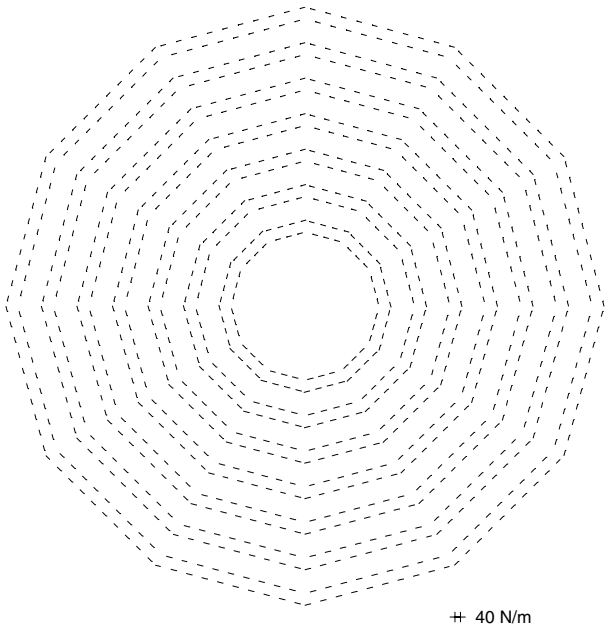

Figure 1.2: Plot of desired prestress magnitudes and directions.

Table 1.1 lists the properties of the offset reflector model.

The approach described above may appear to be at odds with the emphasis, in the two earlier reports on form-finding of CRTS reflectors, on biaxial states of prestress. The reason why we are now prepared to accept essentially uniaxial stress states is because recent work by Wong (2000) has shown that the formation of large amplitude wrinkles in a membrane requires stretching in the direction of the wrinkles. Because of the high stiffness of Kevlar-reinforced foils and of the low level of prestress, wrinkles are not expected to form —despite the lack of

[1]Recall that the reference surface is a cylindrical surface defined by the parabolic ribs of the reflector. It is the reflector shape that is closest to a paraboloid, see Section 1.2 of Lai, You and Pellegrino (1997)

prestress in the meridional direction— provided that the boundaries of each gore are correctly shaped.

Finally, it should be noted that, although the membrane sleeves that enclose the ribs should be located behind the surface, see Rits (1996), for simplicity of manufacture, it was decided to put the ribs above the surface.

Configuration	"Circular" Offset
Diameter (D)	1.5 m
Focal length (F)	0.9 m
Offset (A)	0.35 m
Hub diameter	0.15 m
Number of ribs	12
F/D	0.6
Hoop prestress t_x	40 N/m
Meridional prestress t_y	0.1 N/m
Sag (s)	$D/100$

Table 1.1: Properties of demonstrator, A defined in Fig. 2.2 of Lai and Pellegrino (1999).

1.3 Layout of the Report

This report is laid out as follows.

Chapters 2 and 3 present the design of the key parts of the demonstrator, namely the hub mechanism and the ribs. Manufacturing details are provided for those components that were made specially.

Chapter 4 describes the procedure followed for cutting and joining the membrane, for connecting the edge cable to the membrane and ribs, and for assembling the whole thing.

Chapter 5 describes the procedure followed for packaging the demonstrator according to two different packaging schemes that had been previously investigated. The deployment of the demonstrator, packaged according to both schemes, is investigated using a high-speed camera.

Chapter 6 presents the shape measurement tests that were conducted, and compares the actual surface shape of the demonstrator to the surface that had been designed.

Chapter 7 concludes the report.

Chapter 2

Hub Design

The key functions of the hub are as follows: (i) to provide a stiff interface between the reflector and the spacecraft, probably through a deployable arm; (ii) to impose a smooth, frictionless motion to the ribs by pushing them outwards after the membrane has been deployed; and (iii) to provide an adjustment capability, in case the membrane prestress is found to have decreased after a period of time. It is important, of course, that the size of the hub should be as small as possible because it has a major effect on the packaged size of the reflector.

A significant challenge in the design of the hub is that it needs to apply forces of different magnitudes on the various ribs because of the offset configuration of the reflector.

2.1 Hub Mechanism

Figure 2.1 shows two different designs of the hub mechanism that were considered; only one quarter of the hub is shown in each case. In both designs, the ribs are mounted on linear bearings, mounted radially, and the motion of these bearings is controlled by a series of pulleys and a cable. The key difference between the two designs is in the way the ribs are pushed outwards and the applied forces are controlled.

In design 1, a series of extension coil springs are attached radially to the roots of the ribs; a cable hoop controlled by a motor-driven disk pulls in the ribs when required. However, because each individual rib requires a different amount of force to prestress the membrane, the stiffnesses of the springs need to have the exact values that produce the required variation. This is an unrealistic requirement and hence with this design it would be difficult to apply to each rib its exact force.

In design 2 a cable wrapped round a series of pulleys is used to push the ribs outwards and radial springs are used to pull the ribs inwards when the cable is released. In contrast to design 1, here the rib forces are all related to the cable tension. The amount of force at a particular rib is dependent on the angles between outer and inner pulleys. Therefore, by changing the radii of the inner

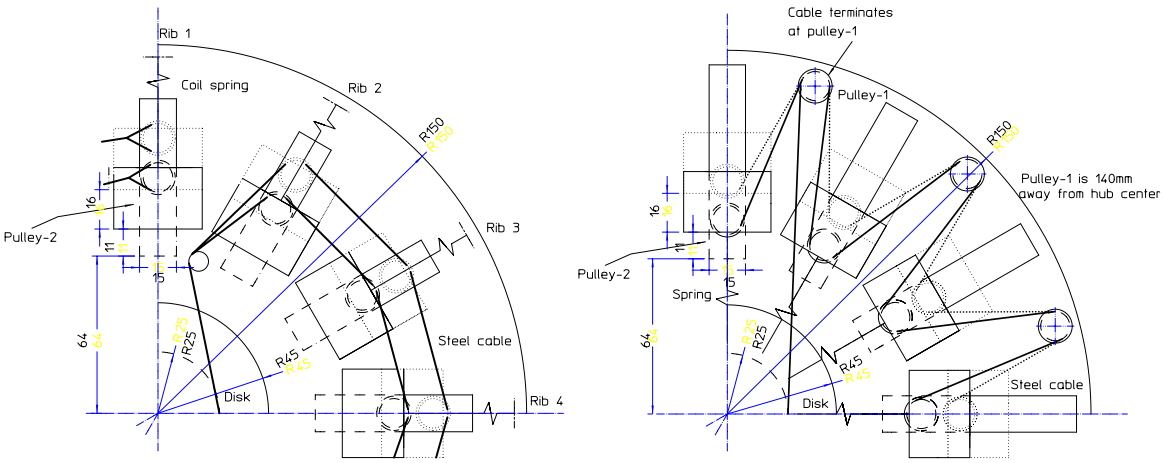

(a) Design 1 (b) Design 2

Figure 2.1: Two hub mechanism designs (dimensions in mm).

pulleys, the required rib force ratios can be achieved quite easily.

It was decided to use design 2 since it is easier to vary the forces applied to the rib while maintaining fixed ratios. Figure 2.2 shows a detailed view of this design, plus a photo of the actual hardware. Each rib is connected to a sliding block, which includes an inner pulley (pulley-1), fixed on a linear guide (carriage/rail). Note that the outer pulleys (pulley-2) holders are fixed. A steel cable loops round all of the pulleys, forming a star shape. At one end, the cable is connected to a central disk, driven by an electric motor, and at the other end the cable is terminated on a fixed pulley.

Detailed design calculations are presented next, and detailed drawings of each component are included in Appendix A.

2.2 Hub Design

The following, key geometrical aspects need to be considered when designing the hub.

2.2.1 Minimum radius

One of the key parameters in the hub design is its diameter. It should be as small as required for the hub to operate correctly; an obvious constraint is imposed by the requirement that the sliding blocks supporting the ribs should not interfere when the ribs are retracted. The minimum radius to avoid contact between

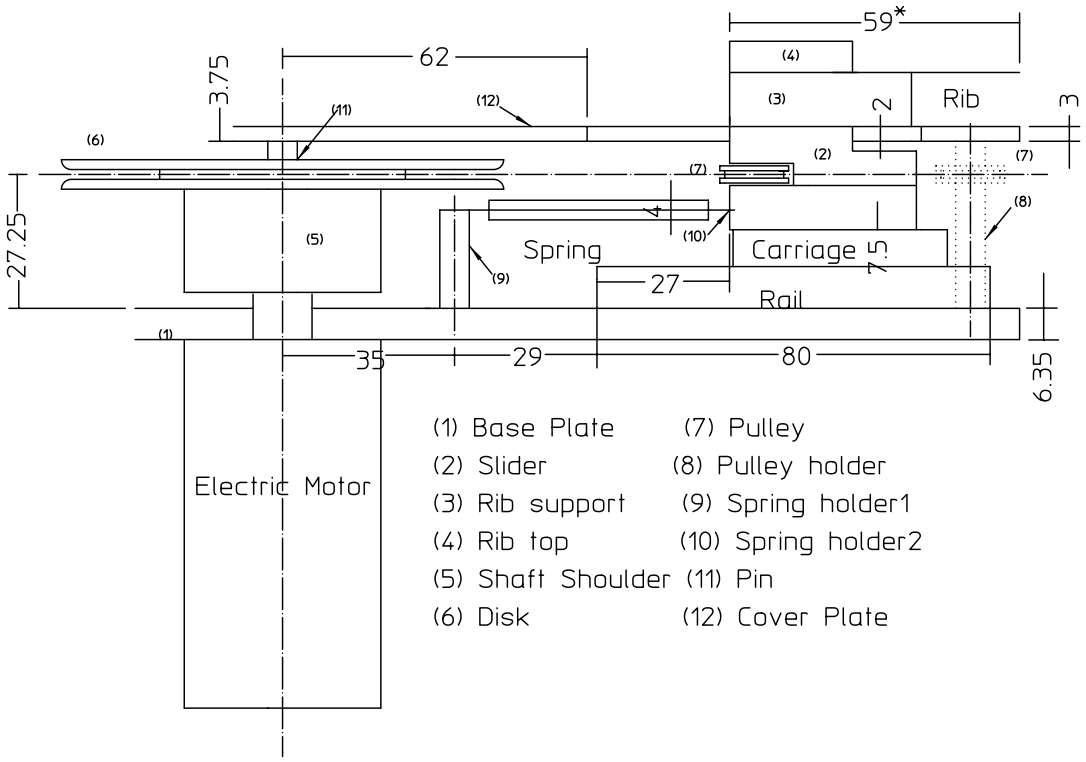

(a) Side view of hub (dimensions in mm).

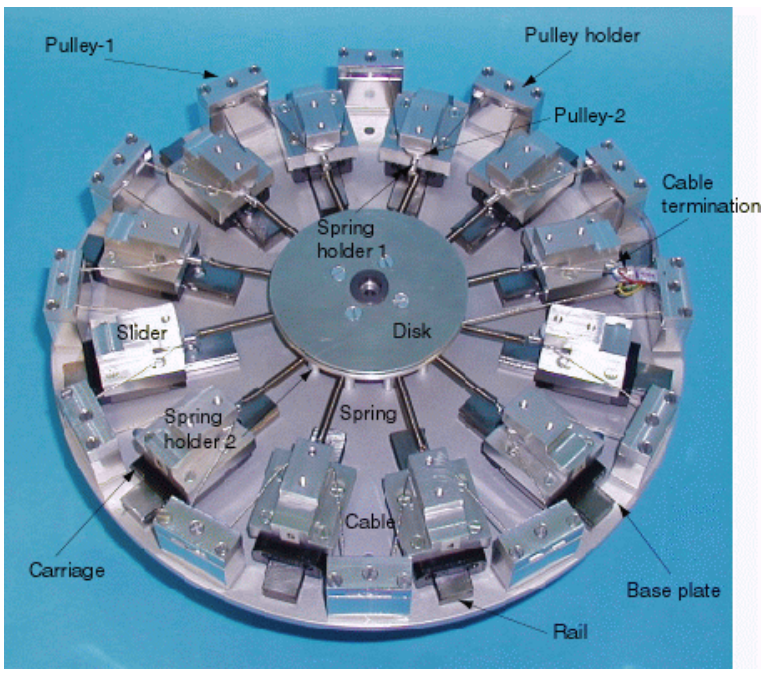

(b) Plan view of the actual hub model.

Figure 2.2: Hub mechanism, below the cover plate.

neighbouring ribs, see Figure 2.3, is

$$R_1 = \frac{w/2}{\tan(\theta/2)} \tag{2.1}$$

where w is the rib width and θ is the angle between the ribs; if the number of ribs is 12, $\theta = 360°/12 = 30°$. From Section 3.1.3 the transverse radius of curvature of the ribs is 22 mm and their subtended angle 120°, hence $w = 39$ mm giving $R_1 = 73$ mm.

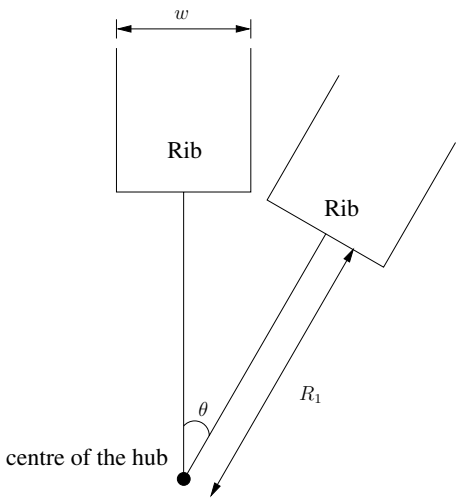

Figure 2.3: Minimum radius R_1.

To the above value of R_1 we add the length of the sliding blocks supporting the ribs, the width of the membrane strip that overlaps with the hub, and also the radial travel of the ribs during prestressing.

A calculation of the elastic displacement that occurs during prestressing gives a very small value, however since preliminary deployment tests on CRTS type reflectors had shown that under certain conditions some of the ribs end up in a reversed configuration after deployment, it was decided to allow enough room for the ribs to be retracted by such an amount that they can then flip into the correct configuration.

Consider, Figure 2.4, the reversed and nominal configurations of a rib. To release the constraint applied by the membrane in these configurations, the root of the rib needs to be retracted by an amount equal to the length of the rib less its horizontal projection, L, hence

$$\delta = \int ds - L = \sqrt{L^2 + \frac{4}{3}H} - L \tag{2.2}$$

δ has different values for the different ribs, because they have different longitudinal curvature. Substituting $L = 600$ mm and the values of H for the various ribs, it is found that δ varies between 6 and 15 mm.

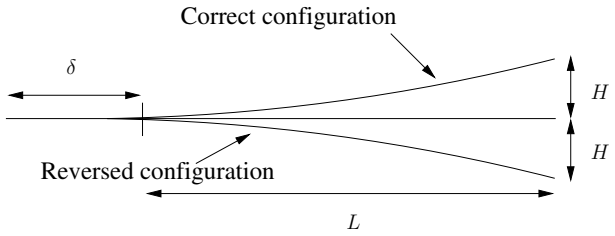

Figure 2.4: Radial movement of a reversed rib to flip back to its correct configuration.

Since the rib support attachment is 25 mm long, see drawing no. 2 in Appendix A, the membrane attachment to the hub is 20 mm wide, see drawing no. 12 in Appendix A, and adding 17 mm for spare, the minimum radius of the hub is $R_{min} = 73 + 15 + 25 + 20 + 17 = 150$ mm.

2.2.2 Radius of pulley-2

As mentioned before, because of the offset configuration, each rib requires a different prestressing force. This was achieved by varying the radii of pulley-2, thus varying the angles between the cable and pulley-2. Figure 2.5 shows a free body diagram of two ribs: F_1 and F_2 are the required forces on ribs 1 and 2; T is the tension in the cable; l_{p1} and l_{p2} are the distances from the centre of the hub to the centre of the pulleys; θ is the angle between the ribs; γ_i are the angles between the cable and lines normal to radii OO_{21} and OO_{22}; r_{ij} is the radius of pulley-i at rib j.

For equilibrium,

$$\begin{aligned} F_1 &= 2T \sin\gamma_1 \\ F_2 &= 2T \sin\gamma_2 \end{aligned} \tag{2.3}$$

Therefore,

$$\frac{F_1}{F_2} = \frac{\sin\gamma_1}{\sin\gamma_2} \tag{2.4}$$

Now consider the pulleys centred at O_{11} and O_{21} and the piece of cable between them, AB , see Figure 2.6

$$\begin{aligned} x_1 &= l_{p1} \sin\theta/2 = L_{T1} \cos\gamma_1 + (r_{21} + r_{11}) \sin\gamma_1 \\ y_1 &= l_{p1} \cos\theta/2 - l_{p2} = L_{T1} \sin\gamma_1 - (r_{21} + r_{11}) \cos\gamma_1 \\ L_{T1} &= \sqrt{x_1^2 + y_1^2 - (r_{11} + r_{21})^2} \end{aligned} \tag{2.5}$$

Here, x_1 and y_1 are the horizontal and vertical components of the distance between the centres of pulley-1 and pulley-2, whose positions are known, O_{11} and O_{21}. Note that γ_1 can be found when l_{p1}, l_{p2}, r_{11}, r_{21} and θ are given.

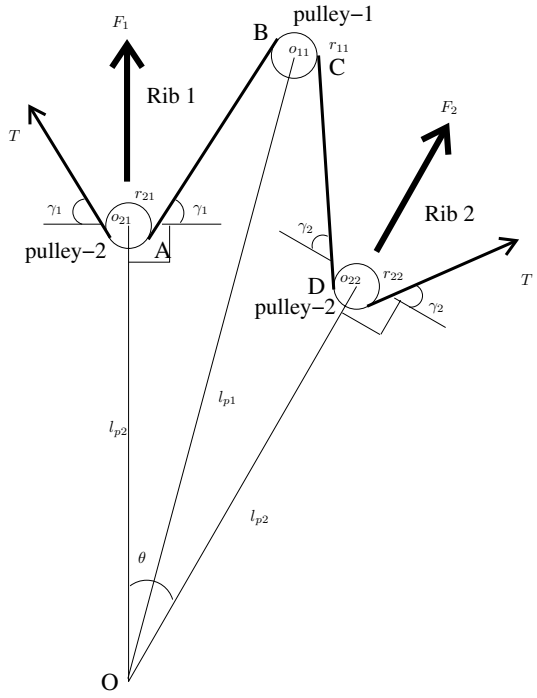

Figure 2.5: Free body diagram of ribs 1 and 2.

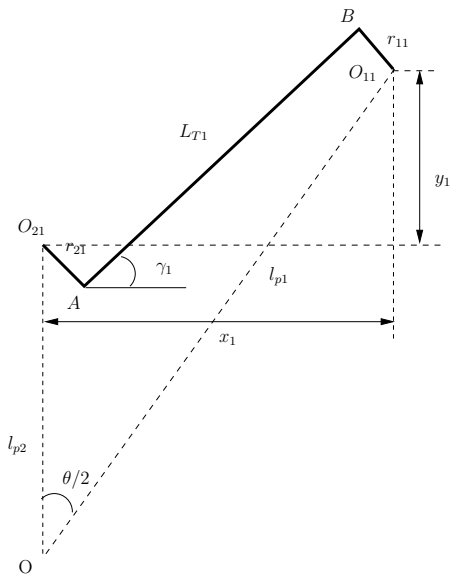

Figure 2.6: Free body diagram of first pulley-2 and pulley-1.

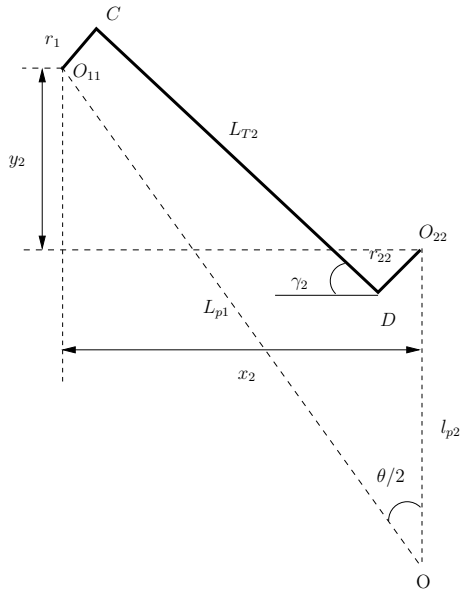

Figure 2.7: Free body diagram of second pulley-2 and pulley-1.

Now consider the pulleys centred at O_{11} and O_{22} and the piece of cable between them, CD, Figure 2.7. An analogous equation to Eqn. 2.5 can be obtained,

$$\begin{aligned} x_2 = l_{p1}\sin\theta/2 &= (r_{11}+r_{22})\sin\gamma_2 + L_{T2}\cos\gamma_2 \\ y_2 = l_{p1}\cos\theta/2 - l_{p2} &= -(r_{11}+r_{22})\cos\gamma_2 + L_{T2}\sin\gamma_2 \end{aligned} \tag{2.6}$$

The radius of all the outer pulleys was chosen to be 6 mm, hence $r_{1j} = 6$ mm. F_1 and F_2 are obtained by analysing the prestressed reflector surface, see Figure 3.7 and Table 3.5. γ_2 can then be found from Equation 2.4 and, substituting into Equation 2.6, r_{22} can be determined. The same approach can be applied to the other ribs to compute the radii of all inner pulleys; Table 2.1 shows their values.

Pulley	Radius [mm]
11-16	6.00
21	6.00
22	5.95
23	5.79
24	5.61
25	5.68
26	5.96
27	6.10

Table 2.1: Radius of pulleys.

2.3 Hub Parts

Many parts of the hub were purchased off-the-shelf, the rest were manufactured in the Workshops of the Engineering Department; drawings of these parts are shown in Appendix A. The materials used were Al-alloy and stainless steel.

The total mass of the complete unit (without ribs and membrane, but including the motor) is 5944 g. It would have been beyond the scope of the present study to optimise the hub, but it is estimated that the total mass could be easily reduced to half or even one third by using different materials and optimising the design of the largest parts. Each component is briefly described next.

Base Plate Supports the whole mechanism and provides a direct attachment point for most components, see drawing no. 1. Mass: 1290 g.

Slider It is machined from a solid Al-alloy block. An inner (pulley-2) is fixed to the back of each slider and is placed on a linear guide. It provides a connection between the rib and the linear guide, see drawing no. 2. Mass: 51 g.

Rib Support and Rib Top Each rib is held between a rib support and a rib top. Both the rib support and the slider have the same transverse curvature as the rib, see drawings no. 3 and 4. Mass: 28 g.

Shaft Connects the output drive shaft with the driving disk, see drawing no. 5. Mass: 112 g.

Disk The disk turns at the same rate as the geared output shaft of the motor. A steel cable wraps around the centre slot in the disk and controls the motion of the ribs, see drawing no. 6. Mass: 75 g.

Pulleys The outer pulleys (pulley-1) are connected to pulley holders. The inner pulleys (pulley-2) are connected to the sliders. The radii of the inner pulleys vary by small amounts, see drawing no. 7.

Pulley Holders Hold the outer pulleys and are located near the edge of the base plate, see drawing no. 8. Mass: 75 g.

Spring Holders Spring holder 1 is connected to the base plate; spring holder 2 is connected to the slider. A soft extension spring links the two holders, and pulls back the rib when the cable is released, see drawings no. 9 and 10.

Pin Provides an attachment point, at the centre of the hub, for the cover plate. It also prevents the disk from wobbling, see drawing no. 11. Mass: 6 g.

Cover Plate Covers most of the hub and provides an attachment for the inner edge of the membrane. Slots in the cover plate allow the sliders, located below the plate, to be connected to the ribs, see drawing no. 12. Mass: 453 g.

The parts which were purchased off-the-shelf are listed in Table 2.2.

Parts	Specification	Purpose	Position
Linear guide (carriage & rail)	LU 15 AL from NSK 66 g, 80 g	To allow smooth deployment of the ribs	On the base plate
Steel geared motor	12 V d.c. 4 r.p.m. 272 g	To drive the centre disk pulling the steel cable	Under the centre of the hub
Small ball bearing	Inner radius 3 mm thickness 4 mm	To allow smooth rotation of the pulleys	Inside the pulleys
Extension spring	Load rate 0.048 N/m	To retract the ribs when necessary	Between spring holder 1 and 2
G Flange bearing	Flange radius 9 mm inner radius 5 mm	To secure the position of the disk	Between pin and disk
Steel cable	0.8 mm diameter	To push the ribs outwards	Wrapped around disk and pulleys

Table 2.2: Parts of the hub purchased off-the-shelf.

Chapter 3

Rib Design

The ribs of the CRTS reflector are similar to a steel tape measure but have a small longitudinal curvature as well, see Figure 3.1. The thickness t_r and tranverse radius of curvature R_r are taken to be uniform. Copper Beryllium (CuBe) and spring steel are the two materials of choice; CuBe was selected because it can be heat-treated at lower temperature , and also it had already been used extensively in our laboratory.

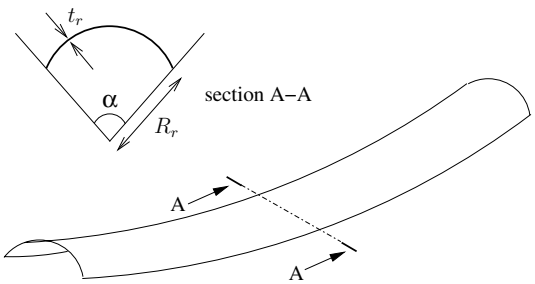

Figure 3.1: Views of doubly curved rib of CRTS reflector.

This chapter begins with a brief summary of the theory of "tape spring" structures, which provides the basis for the design of the ribs of the CRTS reflector demonstrator. After deciding the geometry of the ribs, an experimental study of the shape distortion that occurs during heat treatment was carried out and, finally, the actual set of ribs were manufactured.

3.1 "Strength" Considerations

There are two important parameters that need to be considered in deciding the dimensions of the ribs of a CRTS reflector. They are (i) the maximum bending moment that can be applied by the membrane without buckling the rib, and (ii) the yield limit that governs the folding of the rib when the reflector is packaged.

Figure 3.2 shows a typical relationship between the bending moment (M) and end rotation (θ) for a short length of a longitudinally curved tape spring, based

on Seffen, You and Pellegrino (1997). Note that its behaviour is different for different signs of the bending moment. In the bottom-left-part of the diagram, a negative bending moment applies compressive stresses to the edge of the tape spring. In the right-hand-part a positive bending moment is applied, and hence the stresses on the edge are tensile. Therefore, the buckling moment is much higher for positive bending, i.e. $M^+_{max} >> |M^-_{max}|$.

Note that for both positive and negative bending M becomes constant when $|\theta|$ is sufficiently large (typically around 10° or so. In this range the deformation of the tape spring is localised in a short, longitudinally curved region and when $|\theta|$ is further increased all that happens is that the length of this curved region increases. In effect, this region behaves like a *constant moment elastic hinge*.

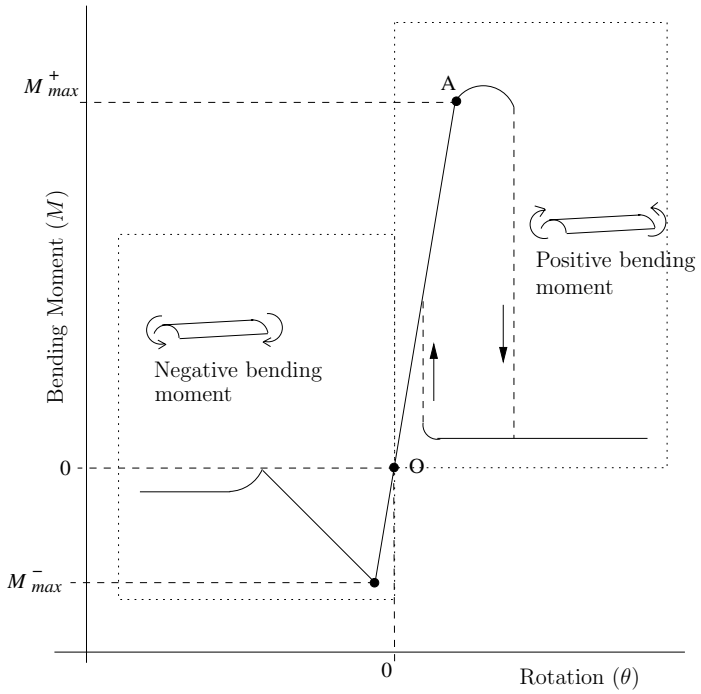

Figure 3.2: Typical moment-rotation relationship of a rib.

3.1.1 Buckling

Because $M^+_{max} >> |M^-_{max}|$ in a tape spring, the ribs of the CRTS reflector are arranged such that the loading from the membrane surface induces a positive bending moment. Hence, they are placed with their convex side facing towards the focus of the paraboloid.

The maximum bending moment in the ribs due to the load applied by the prestressed membrane must be lower than the buckling moment (M^+_{max}) of the rib. The ribs were designed for an assumed prestress level in the membrane of $t_x = 40$ N/m and $t_y = 50$ N/m, which results in a maximum bending moment of 1.5 Nm, see Section 3.1.3. However, it was later decided to lower the prestress to

$t_x = 40$ N/m and $t_y = 0.1$ N/m, see Table 1.1, and thus the safety margin against buckling became considerably higher.

Seffen and Pellegrino (1997) obtained the following approximate expression for the buckling moment for positive bending of a straight tape spring

$$\frac{M^+_{max}}{D} = A'\alpha^m \tag{3.1}$$

where α is the angle subtended by the cross-section of the rib and

$$\begin{aligned} D = &\quad \frac{Et_r^3}{12(1-\nu^2)} \\ A' = &\quad \frac{R_r}{t_r}\left[1.152\times10^{-3} - \frac{2.210\times10^{-3}}{l}\right. \\ &\quad \left. + \left(-2.061\times10^{-9} + \frac{7.096\times10^{-6}}{l_r^4}\right)\left(\frac{R_r}{t_r}\right)^2\right]^{0.5} \\ m = &\quad 2.840 + \frac{18.170}{l_r^2} \\ &\quad + \left[-2.281\times10^{-3} + \frac{6.809\times10^{-2}}{l_r} - \frac{0.245}{l_r^2}\right]\frac{R_r}{t_r} \end{aligned}$$

where t_r, l_r and R_r are respectively the thickness, length, and cross-sectional radius of curvature of the rib, E and ν are its Young's Modulus and Poisson's ratio.

A longitudinally curved tape spring has M^+_{max} approximately equal to a straight one, for which the above results were obtained. Hence, Eq. 3.1 can be used to produce a quite an accurate estimate of M^+_{max}.

3.1.2 Yield Limit

The ribs may deform plastically if the bending stresses that occur during folding are too high; of course, this would not be acceptable. Seffen and Pellegrino (1997) have analysed the biaxial stress state in the elastic fold region of a straight tape spring, and have shown that the following condition has to be satisfied to avoid plastic yielding

$$\frac{R_r}{t_r} \geq \frac{E}{\sigma_y(1+\nu)} \tag{3.2}$$

where σ_y is the yield stress of the material.

"Brush annealed CuBe alloy 165" was selected from the Brush Wellman catalogue. Its physical and mechanical properties are listed in Tables 3.1 and 3.2; Ssubstituting the values of E, σ_y, ν from these tables into Equation 3.2 gives

$$R_r/t_r \geq 91.6 \tag{3.3}$$

for elastic behaviour. Considering the commercially available thicknesses of this alloy, we obtain $R_{min} = 9.16$ mm for t_r=0.1 mm and $R_{min} = 18.4$ mm for t_r=0.2 mm.

Density	8400 kgm^{-3}
Young's Modulus, E	131×10^9 Nm^{-2}
Poisson's ratio, ν	0.3
Thickness, t_r	0.1 or 0.2 mm
Melting Point	871 – 982 °C

Table 3.1: Physical properties of CuBe 165 alloy.

	Ultimate Tensile Stress, σ_{max}	Yield Stress, σ_y
Annealed	500 Nmm^{-2}	200 Nmm^{-2}
After aging 3 hrs at 316 °C	1200 Nmm^{-2}	1100 Nmm^{-2}

Table 3.2: Mechanical properties of CuBe 165 alloy.

3.1.3 Rib Dimensions

Table 3.3 shows a list of feasible rib dimensions with their buckling moments M^+_{max}, obtained from Equation 3.1 for $l_r \approx 750$ mm.

As mentioned above, the maximum bending moment applied to the ribs is around 1.5 Nm and, taking a safety factor of 2, we looked for ribs capable of carrying moments up to around 3.0 Nm. The finally chosen configuration was: $t_r = 0.2$ mm, $R_r = 22$ mm and $\alpha = 120°$. This configuration meets the strength requirements, but may lead to ribs that are too stiff. Hence, it was decided to adopt a tapered design, with $\alpha = 90°$ at the tip and $\alpha = 120°$ at the root. Table 3.4 shows the corresponding values of M^+_{max} along the length of this rib.

3.2 Design of Rib Moulds

The ribs were made from flat strips of 0.2 mm thick annealed CuBe, pressed into a steel mould and then heat-treated in a furnace to age-harden the alloy, thus increasing its hardness.

Because of the offset configuration of the reflector, there are a total of seven different ribs, namely the two ribs lying in the plane of symmetry plus five pairs. Hence, several different moulds are required.

3.2.1 Shape Distortion during Heat Treatment

Heat treatment of CuBe involves the metallurgical precipitation of a hard beryllide phase within a copper alloy matrix. This hard phase has a higher density than the matrix, and its formation at elevated temperature leads to a slight volume change during the heat treatment cycle. The volume change is negative, which means that the density increases.

If the volume change occurs uniformly throughout the mechanical part that is

t_r [mm]	R_r [mm]	α [deg]	M^+_{max} [Nm]
0.1	18	160	1.7
	19	160	1.8
	20	150	1.6
	21	150	1.7
	22	140	1.4
		150	1.9
	23	140	1.5
		150	2.0
0.2	18	120	2.4
		130	3.1
	19	120	2.6
		130	3.3
	20	120	2.7
		130	3.5
	21	120	2.9
		130	3.8
	22	**120**	**3.1**
		130	4.0
	23	120	3.3
		130	4.3

Table 3.3: Possible rib configurations; chosen configuration in bold.

α [deg]	M^+_{max} [Nm]
120	3.1
110	2.3
100	1.7
90	1.3

Table 3.4: M^+_{max} along tapered rib with $R_r = 22$ mm and $t_r = 0.2$ mm.

being heat treated, its density would increase uniformly, and so the overall shape of the part would not be affected. On the other hand, if the volume change is not uniform, shape distortion can occur. The most likely cause of shape distortion of a thin strip of CuBe during heat treatment is the existence of non-uniform stresses resulting from bending of the strip.

For example, the flat strip shown in Fig. 3.3(a) is pressed into a curved mould that induces compressive stresses on the inside of the bend and tensile on the outside. The volume contraction that occurs during heat treatment is intensified by the compressive stresses and, correspondingly, tensile stress retard the process. Thus, after heat treatment the strip will be more curved than the mould, see Fig. 3.3 (b).

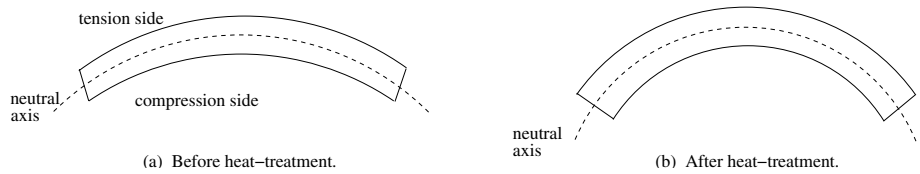

Figure 3.3: Shape distortion during heat treatment.

3.2.2 Transverse Curvature of Moulds

Because of the shape distortion that occurs during heat treatment, the tranverse radius of the rib mould R_m must be greater than the required transverse radius of the ribs $R_r = 22$ mm.

A trial and error approach was adopted to determine the transverse radius of the mould which is required to produce $R_r = 22$ mm. Three cylindrical steel moulds with radii of 22 mm, 27 mm and 32 mm, see Figure 3.4, were made. Four CuBe strips were heat-treated in each mould and their radii were measured afterwards. Figure 3.5 is a plot of the measured radii against the corresponding mould radii. A straight line fitted to this data gave a mould radius R_m=31 mm for $R_r = 22$ mm.

3.2.3 Longitudinal Curvature of Moulds

The ribs of the CRTS reflector are also longitudinally curved and a similar trial and error approach was used to find the longitudinal profile of the moulds. Two steel moulds with different curvatures were made, as shown in Figure 3.6. It was found that, because the longitudinal curvature is much smaller, the shape distortion during heat treatment is effectively negligible.

To determine the shape in which the ribs should be manufactured, the deformation due to the forces applied by the membrane needs to be taken into account. A rib is modelled as a cantilever beam and, starting from its "operational configuration", forces opposite to those applied by the membrane are applied and the

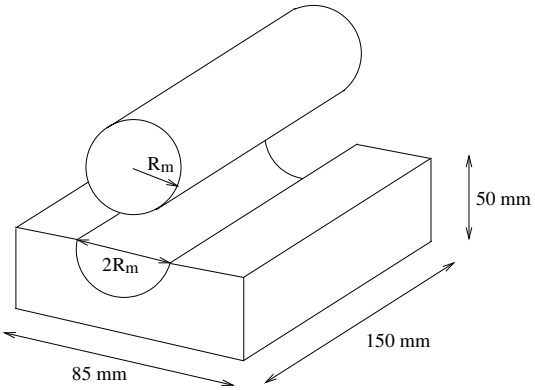

Figure 3.4: Cylindrical mould.

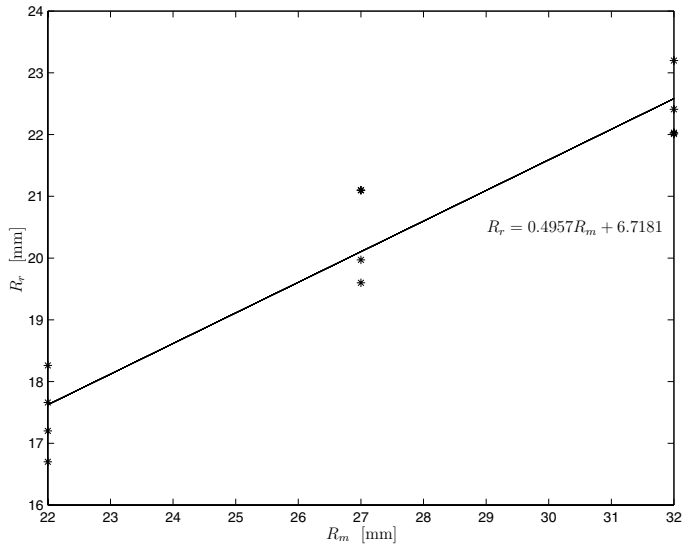

Figure 3.5: Change of transverse radius during heat treatment.

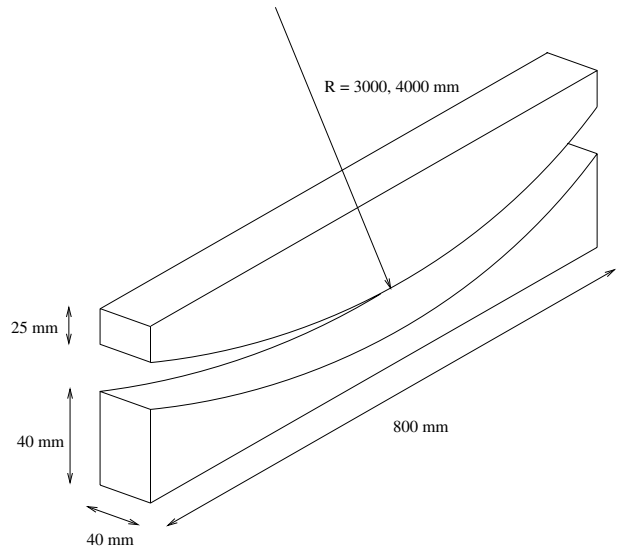

Figure 3.6: Mould with longitudinal curvature only.

deflected shape is computed. Provided that this deflection is sufficiently small, this deflected shape is precisely the shape in which the rib should manufactured. The seven different rib configurations of the CRTS were determined in this way.

Figure 3.7 shows the loads applied along each rib by the membrane and edge cable; note that all the loads are horizontal and, apart form the tip load, uniform. The corresponding deflections are also shown in the figure. Table 3.5 lists the bending moments and the axial forces, compressive of course, at the root of each rib. Note that the rib loads are almost identical and the highest bending moment is at rib 7. The distribution of the bending moment in rib 7 is shown in Figure 3.8.

Rib number	Bending moment at root [Nm]	Axial force [N]
1	0.68	12.52
2	0.63	12.51
3	0.52	12.49
4	0.44	12.46
5	0.49	12.47
6	0.66	12.51
7	0.76	12.53

Table 3.5: Bending moment and axial force at the root of each rib.

Although each rib profile is different from the others, this variation is not very great because the CRTS reflector model does not have a large offset. Also, there is always a small difference between the desired shape and the shape that

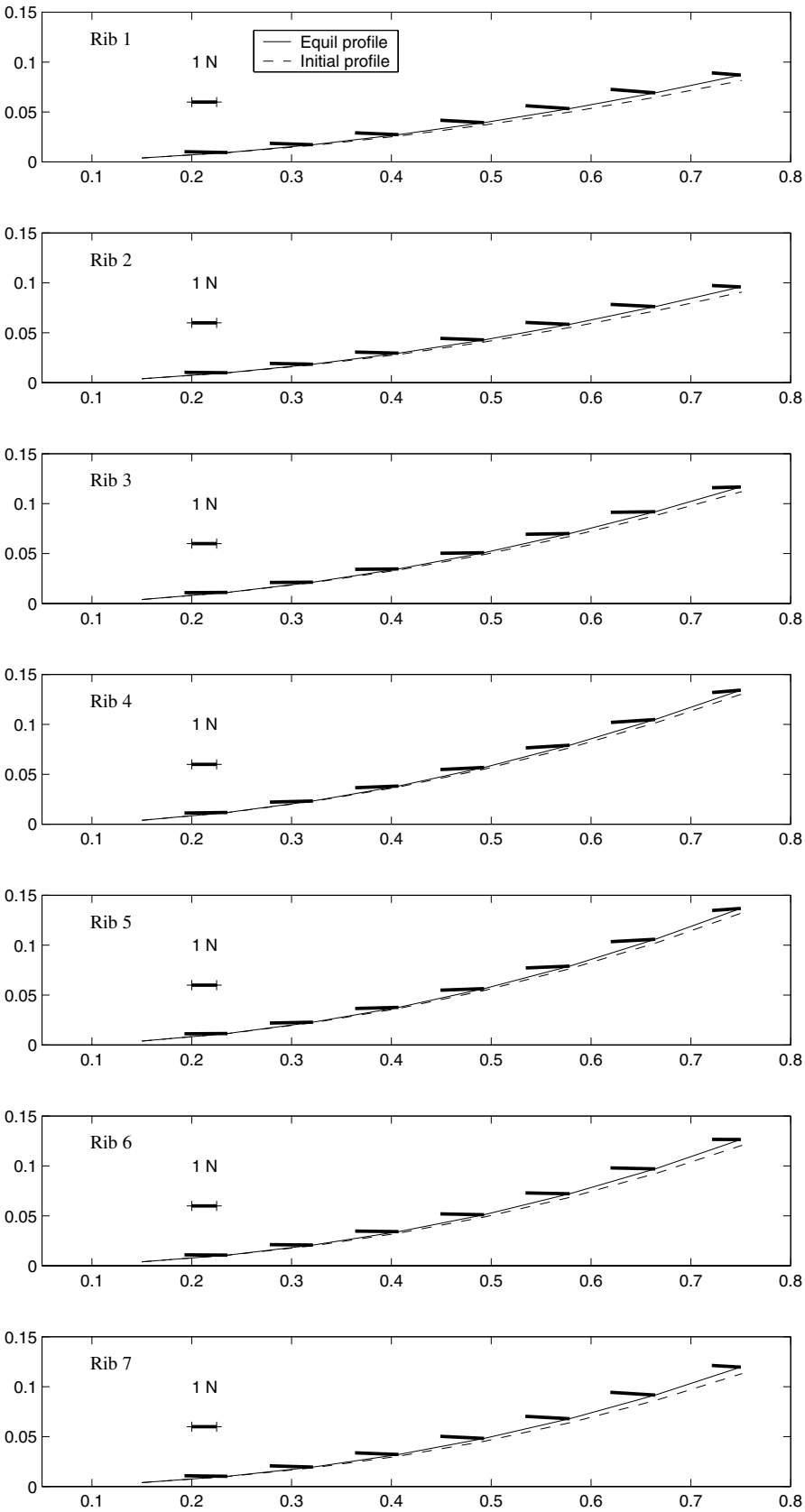

Figure 3.7: Load distribution and corresponding deflections of ribs.

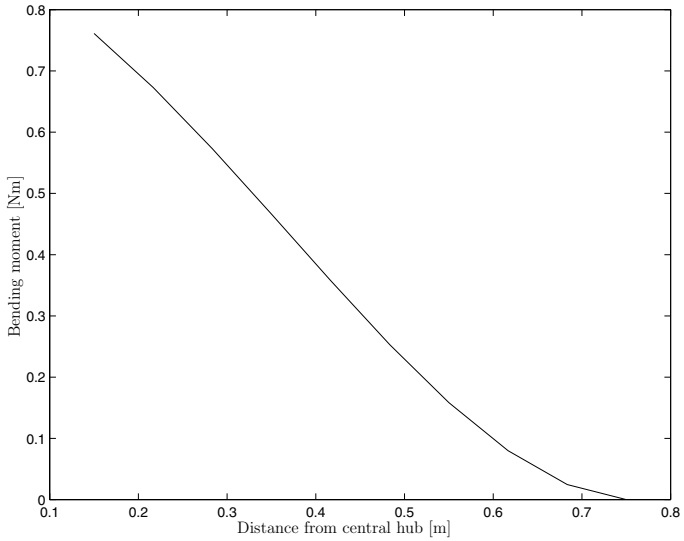

Figure 3.8: Bending moment distribution along rib 7.

is actually obtained after heat treatment. Therefore, since each mould requires a lot of time to be made, it was decided to use the same mould for rib profiles that are reasonably similar.

Figure 3.9 compares the initial profiles of the ribs, taken from Fig. 3.7. It is clear that the profiles of ribs 4 and 5 are virtually the same, and those of rib 6 and rib 3 are also very close. Therefore, the number of rib moulds can be reduced from seven to five.

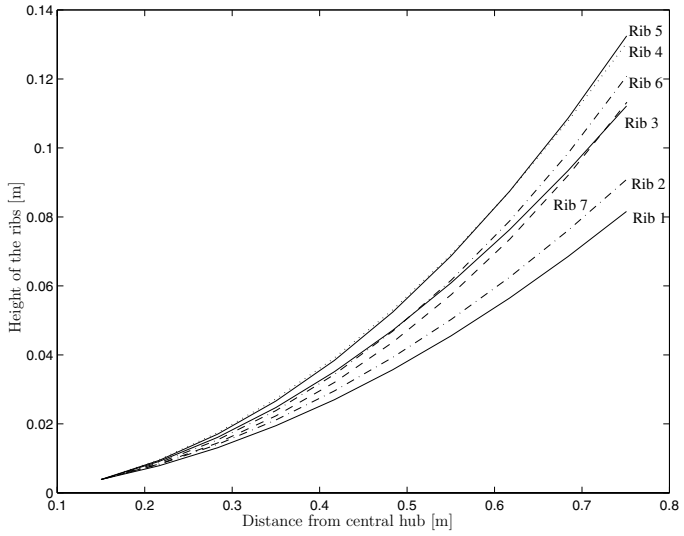

Figure 3.9: Initial rib profiles.

The rib profiles discussed so far have not included the additional length re-

quired for the end connections; in practice the ribs need to be made longer. Figure 3.10(a) shows how to extend the profiles obtained above, to find the complete shape that needs to be manufactured with a CNC machine. The solid line between points 3 and 4 represents the profile obtained from the above computational analysis, then a second order polynomial curve is fitted, represented by a dashed line and the curve is thus extended from point 1 to 5. The distance between points 2 to 3 corresponds to the length that overlaps with the sliding block. The distances between points 1 and 2, and points 4 and 5 are spare lengths.

Before manufacturing, the whole rib is rotated to reduce the thickness of the mould and hence the amount of material required. Figure 3.10 (b) shows the longitudinal profiles obtained thus. It can be seen that the maximum difference between the profiles of rib 1 and 2 is around 1-2 mm when they are overlapped at points 2 and 4; similarly for rib 3, 6 and 7 the maximum difference is about 3 mm. Since the expected accuracy of the heat-treatment is also around 3 mm, it was decided to make three moulds only, i.e. moulds 1, 3 and 5.

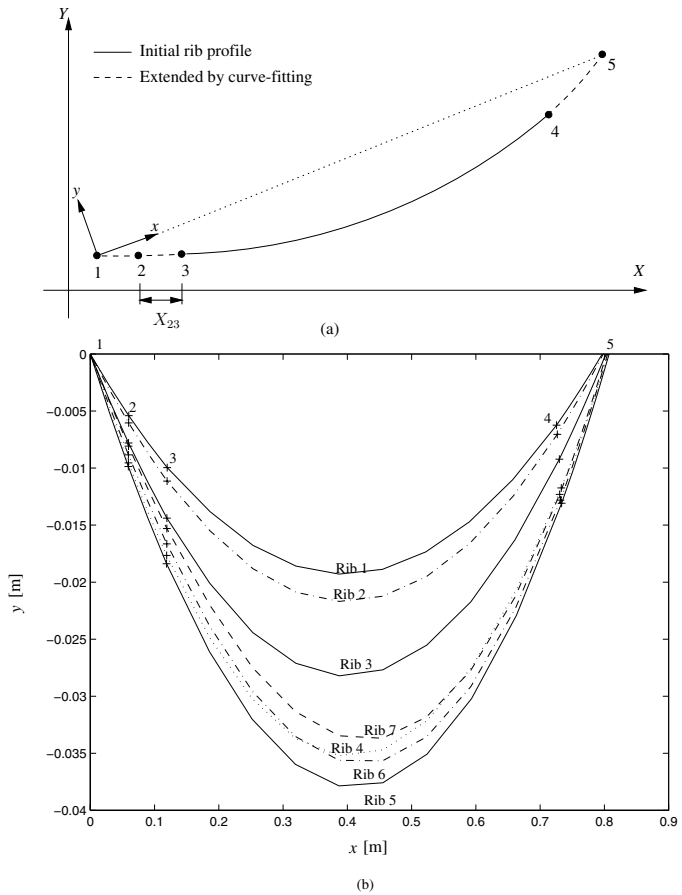

Figure 3.10: (a) Extended rib profile and (b) longitudinal profiles of rib moulds.

Figure 3.11 shows a sketch of a rib mould. It consists of separate male and female parts, machined from mild steel blocks with a CNC machine. The two

parts have matching longitudinal and transverse curvatures with 0.2 mm offset for fitting the CuBe strip tightly between them.

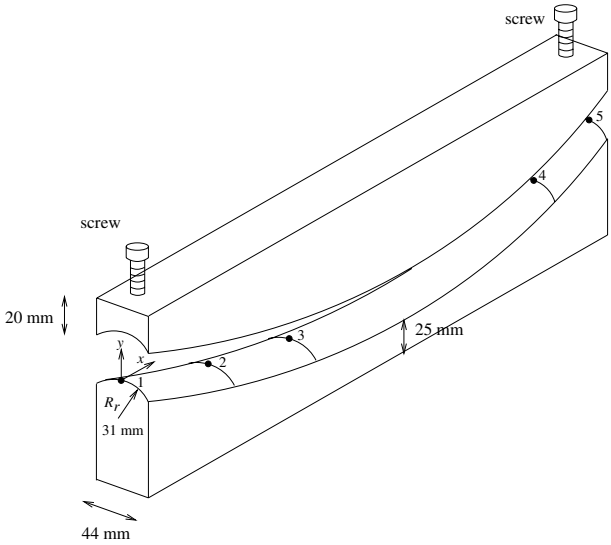

Figure 3.11: Doubly curved rib mould.

Along the mould, there are three marks that indicate the position in which the CuBe strip has to be placed on the mould. The machining error of the mould surfaces was checked with a Mitutoyo EURO-M544 coordinate measuring machine. The maximum deviation was found to be 0.11 mm.

3.3 Manufacture of Ribs

The heat treatment of each rib was carried out as follows. A flat tapered strip of CuBe was cut with a guillotine from a 0.2 mm thick sheet; Fig. 3.12 shows the dimensions of this strip.

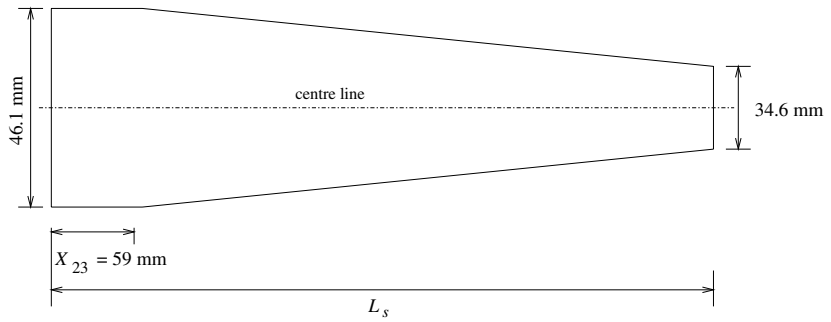

Rib no.	L_s [mm]	Mould no.
1	665.4	1
2	666.9	1
3	670.8	3
4	675.0	5
5	675.9	5
6	673.6	3
7	672.1	3

Figure 3.12: Dimensions of tapered CuBe strip.

It was found that sometimes the guillotine bends the edges of the strip and the associated residual stresses result in the shape of the rib being twisted after

the heat treatment. This can be avoided by sanding and polishing the edges of the strips, which also rounds the edges of the ribs and so reduces the risk that they might cut the membrane while sliding within the membrane pocket.

The CuBe strip was carefully placed on top of the male part of the mould, between the points marked 2 and 4 in Fig. 3.11, and its position was secured with a few drops of super glue. Then, the female part of the mould was put on top of the male part and the two parts were pressed together by tightening the screws at both ends. A stiff spring was placed under each screw to maintain a uniform pressure during heating of the mould. The mould was then put into a vacuum furnace, at a temperature of 316°C for three and a half hours,[1] and then the furnace was allowed to cool down to room temperature.

[1]Note that heat treatment time had been extended by half an hour to allow for the heating of the furnace and the mould.

Chapter 4

Construction of Demonstrator

Useful lessons had been learnt earlier on, by putting together a small scale physical model which aimed to model only one gore of a symmetric reflector (Lai, You and Pellegrino 1997). Hence, the procedure that was followed in constructing the 1.5 m offset CRTS demonstrator tried to avoid all the pitfalls of the earlier procedure. In particular, it had been found that even small geometrical incompatibilities between the rib and hub attachments of the membrane can lead to the formation of wrinkles in this region. This time the alignment of all parts was checked very carefully, both when designing the hub and after all the parts had been made.

4.1 Cutting the Membrane

Kevlar-reinforced Kapton foil, previously developed by ESTEC and Contraves in connection with the inflatable, space-rigidised technology (Bernasconi and Rits, 1990) was used. This foil had already been used for the preliminary tests described in Lai, You and Pellegrino (1997); its properties are listed in Table 4.1.

Thickness	0.1 mm
Density	79 g/m^2
Young's Modulus	11.9×10^3 N/mm^2
Poisson's ratio	0.3

Table 4.1: Properties of Kevlar-reinforced Kaption foil.

The membrane surface is formed by twelve gores, whose shapes are generated according to the computational analysis in Sections 2.5 and 3.2.2 of Lai, You and Pellegrino (1997). Since it had been decided that the prestress distribution in the offset CRTS demonstrator would be purely in the "hoop direction", as shown in Fig.1.2, the equilibrium surface and the actual surface coincide with the reference surface. Hence, the surface of the reflector consists of twelve flat elements, whose shapes are computed by de-stressing the prestressed surface, disconnecting the

gores, and then flattening them. Due to the existence of a plane of symmetry, the cutting patterns of corresponding gores are identical, hence only six cutting patterns had to be computed.

Six 2 mm thick Al-alloy templates were then made with a CNC machine. One of these profiles is shown in Fig. 4.1; note that the out-of-straightness of the edges is only about 2 mm over their full length.

The membrane was laid flat on a soft rubber pad and a small amount of water was used to hold it on the template; this produces a bond sufficient to prevent the membrane from moving while it is being cut. Then the edge profile was cut by hand, with a very sharp blade, using a magnifying glass.

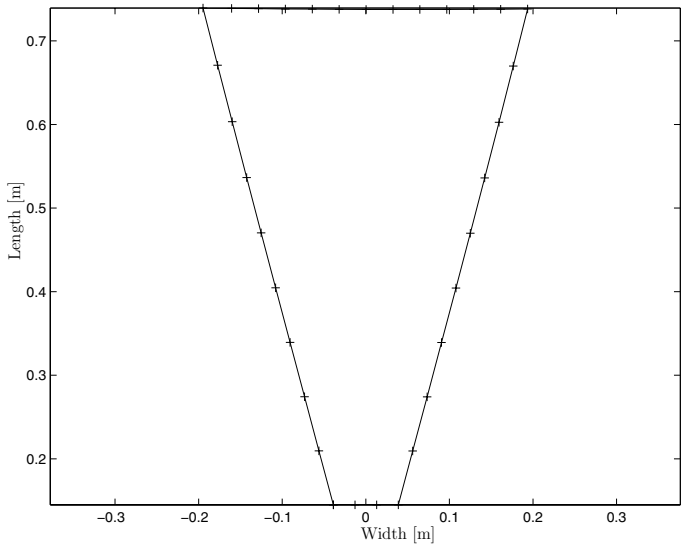

Figure 4.1: Cutting pattern for a membrane gore.

4.2 Joining the Membrane

All connections between the pieces of membrane were made with Polyimide adhesive tape bonded to the aluminised side of the membrane (the tape does not stick to the Kevlar). Because the edges of the gores are not exactly straight, each gore needs to be placed on a cylindrical surface for the edge to lie in a plane. Hence, adjacent gores were placed side-by-side on curved timber moulds and firmly held at the narrow ends with double-sided tape, before they were bonded together.

Each rib was located inside a rib sleeve —made of the same Kevlar-reinforced Kapton foil— that had been previously bonded, also with Polyimide tape, to the membrane on either side of the seam between adjacent gores.

A 1 mm diameter Kevlar cord covered by a Nylon sheath was arranged to form a loop around the perimeter of the membrane, 6 mm from the edge see Fig. 1.1, and was connected to the membrane with adhesive tape.

4.3 Terminations

The root of each rib was placed between the rib top and rib support elements, see Section 2.3, and connected to the corresponding sliding block with two screws. Figure 4.2 shows the tip end of a rib sleeve. The sleeve is bent over and bonded along the edges using Polyimide tape; this forms a pocket against which the rib can push, when the hub is expanded.

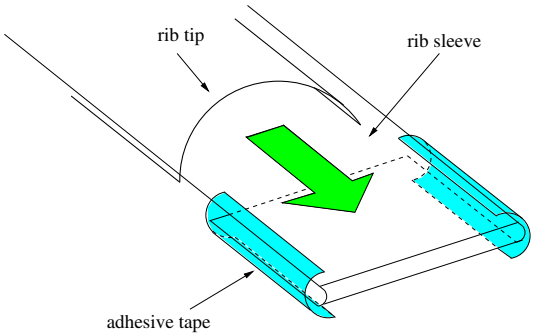

Figure 4.2: Rib sleeve termination.

The cable around the outer edge of the reflector surface is looped through a series of holes at the tip of each rib and terminates on a tensioning screw, connected to the tip of rib 1. Figure 4.3 shows a detailed view of the connection between this edge cord and rib 1. Holes A, B, D, E —at the tips of each rib— have a diameter of 1.5 mm; hole C —only at the tip of rib 1— has a diameter of 2 mm. A nut soldered underneath this hole holds the tensioning screw.

When the cable reaches a rib, it is looped through hole A, then through holes B and D, and finally comes out of hole E before continuing along the edge of the next gore. At rib 1, the two ends of the cable come out of holes B and D and are attached to the tensioning screw. The nylon sheath that covers the Kevlar cord is removed, before connecting the cord to the screw with super glue, so that the cable can be tensioned simply by turning the screw.

Note that this very lightweight termination of the edge cord, much lighter and simpler than that used by Lai, You and Pellegrino (1997), relies on the cross-section of the rib being sufficiently rigid at the tip. In the CRTS demonstrator the cable tension is so low that this is not a problem, but an end stiffener could be attached to the tip of the rib, if required.

4.4 Assembly of Demonstrator

The hub mechanism was assembled as follows, see Fig. 2.2 to better understand the description. First, the DC motor was attached under the centre of the base plate, then the linear guides, pulley holders with pulleys, and the spring holders-1, were also attached to the base plate. Care was taken in arranging the pulleys

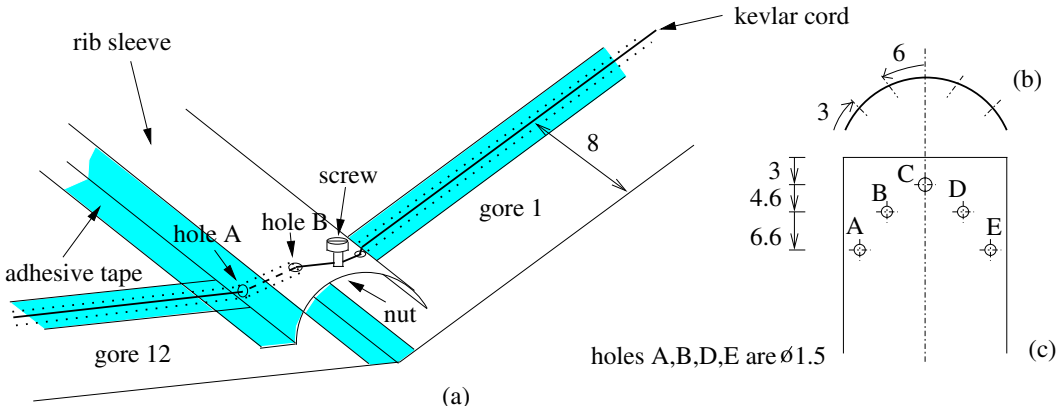

Figure 4.3: Rib end termination; (a) perspective view; (b) end view and (c) top view of rib (all dimensions in mm).

according to their diameter, as required to apply the correct prestressing forces to the ribs; spring holders-2 were attached to the carriages of the linear guides. The extensional springs were then placed between the spring holders. A 1.0 m long steel cable was connected to the centre of the driving disk, previously mounted on the shaft, and connected to the output shaft of the motor. The height of the disk above the base plate was adjusted to match the height of the other pulleys. The cable was terminated on one of the pulley holders, as shown in Fig. 2.1(b). Finally, the pin was placed on the disk and the cover plate was attached.

Next, the complete membrane surface, with the ribs inside the sleeves and connected at the tips through the Kevlar cord, was put over the cover plate of the hub. Each rib was placed between the rib support and rib top, and secured with screws to the corresponding slider. This completed the assembly of the demonstrator. At this point the DC motor was turned on and the steel cable was wound onto the disk, until the correct tension value had been reached.

Figure 4.4 shows two photos of the demonstrator, taken from viewpoints roughly perpendicular to the plane of symmetry but at different heights. The shallower ribs are to the right. Note that the aluminised surface shines and even very small undulations are clearly visible in the photo.

In fact, the surface is really quite smooth, as clearly shown by the end view of a gore, in Figure 4.5. The smoothness of the surface is also confirmed by the photo of the back of the surface, Figure 4.6, covered with Kevlar fibres. Figure 4.7 is a detailed view of the connections between the ribs and the membrane, above the hub.

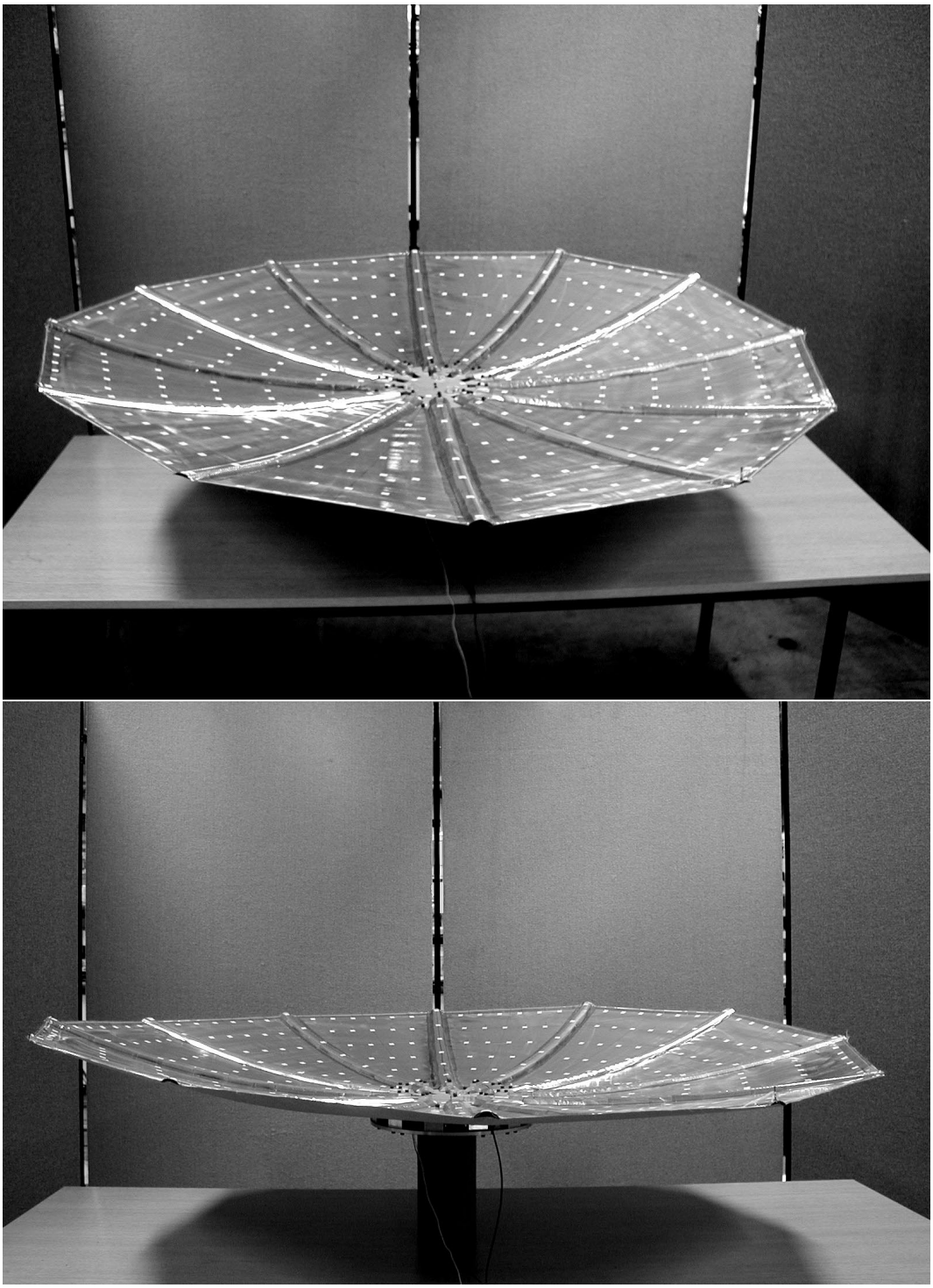

Figure 4.4: Photos of completed demonstrators.

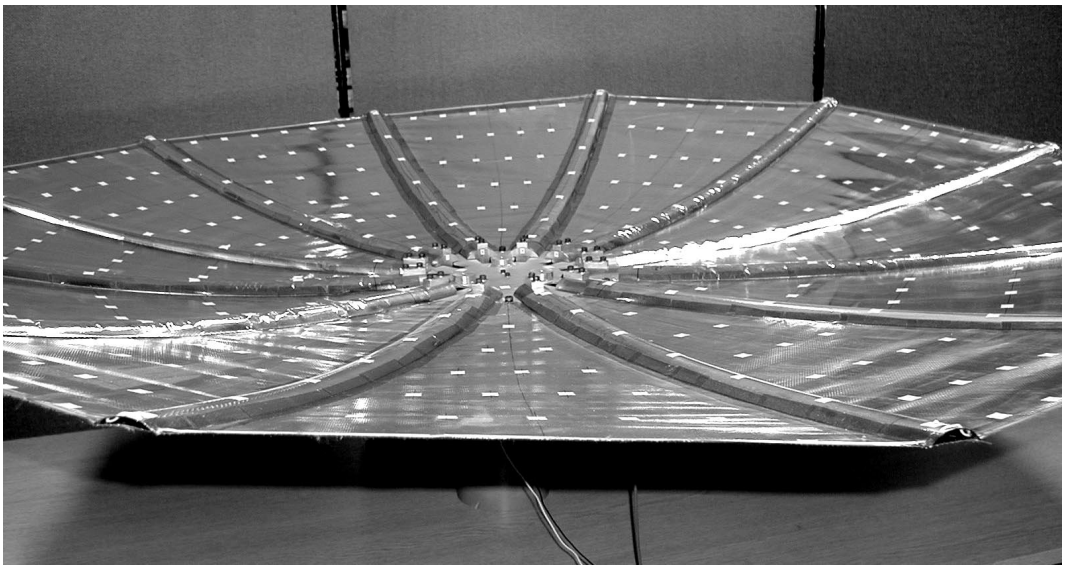

Figure 4.5: View of gore 4.

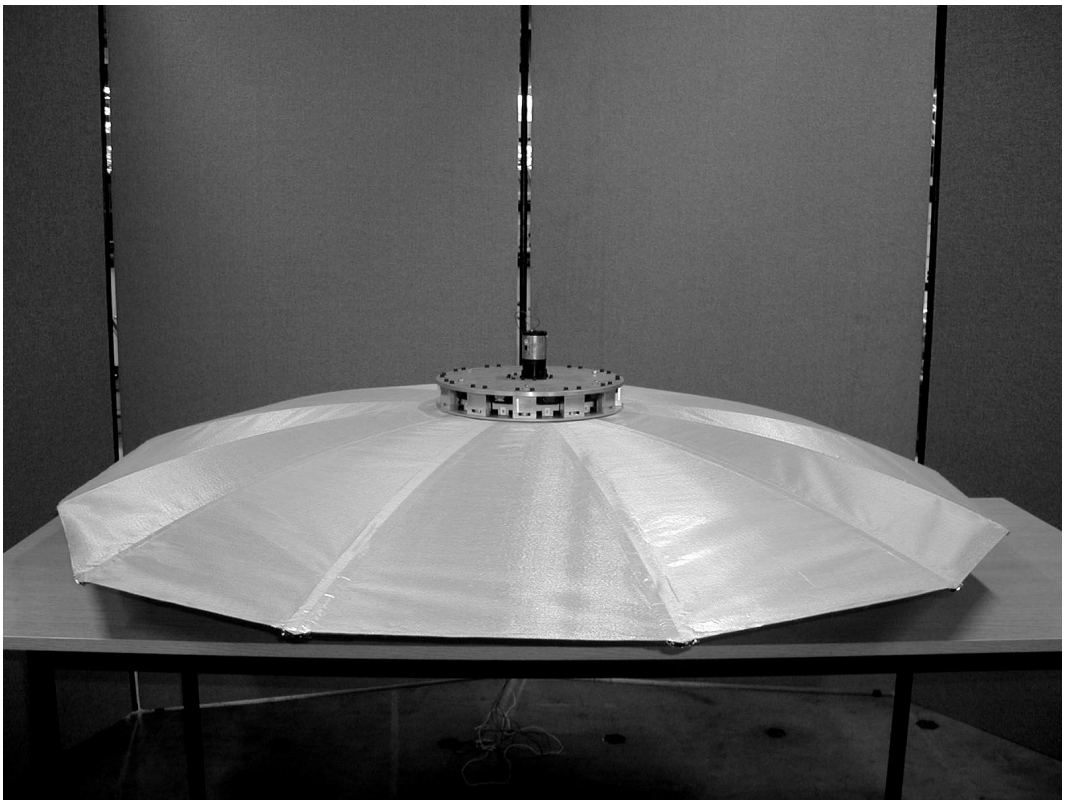

Figure 4.6: View of the back of the reflector.

Figure 4.7: Hub connection between hub and membrane.

Chapter 5

Packaging and Deployment Tests

Packaging schemes for CRTS reflectors were first investigated by You and Pellegrino (1994). Two different packaging schemes were identified for reflectors with straight ribs: zig-zag folding, with each rib folded up and down in its own plane, as shown in Fig. 5.1, and wrapping, with the ribs bent and twisted around the hub, as shown in Fig. 5.2.

As part of the present effort, Seffen, You and Pellegrino (1997) have investigated the elastic folding and deployment dynamics of curved ribs. They found that curved ribs can be folded by forming localised elastic folds with a longitudinal radius of curvature approximately equal to the transverse radius of the ribs, much in the same way as straight ribs. Therefore, the same packaging techniques proposed for reflectors with straight ribs can also be applied to reflectors with curved ribs.

Seffen et al. also found that the deployment dynamics of curved ribs with *positive folds*, i.e. those obtained by applying a positive bending moment, recall Fig. 3.2, are very similar to the dynamics of straight ribs. However, *negative folds* are bi-stable, and so a rib of a CRTS reflector that is folded downwards can be in equilibrium under zero external moment both in the fully-deployed configuration and in a partially folded configuration. Hence, the zig-zag packaging technique is not entirely reliable, because it relies on the inertia forces associated with the dynamics of deployment for preventing the ribs from stopping half-way through.

This chapter presents deployment tests that were carried out with the demonstrator packaged according to the two folding schemes. In order to avoid damaging the high precision membrane, the model was set up with a membrane made of 0.09 mm thick Kapton foil, with the same cutting pattern of the membrane described in Section 4.1, and a preliminary set of ribs. After the deployment test, both the membrane and the ribs were replaced, before measuring the shape of the surface. A perspex cylinder with the same diameter of the hub was placed above the hub, forming a rigid support against which the ribs and the membrane could be folded.

In each test, the deployment sequence was recorded with a Kodak Ektapro 4500 high-speed digital camera, set at 250 frames per second. To eliminate blur-

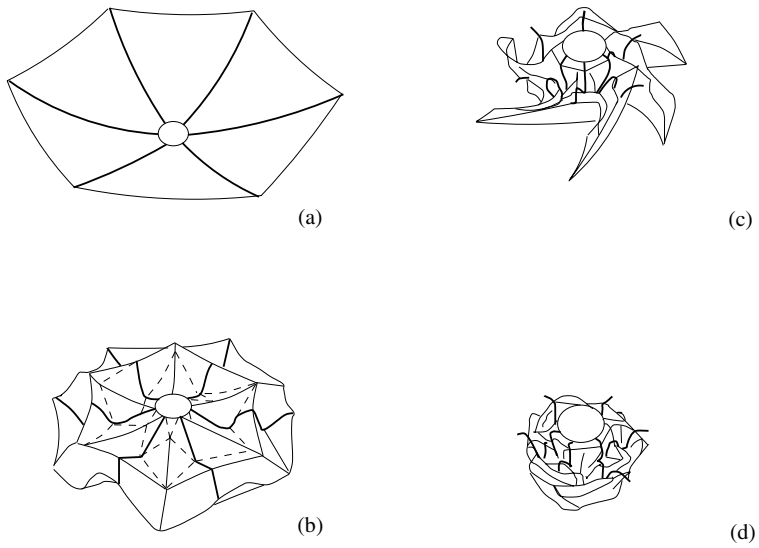

Figure 5.1: Zig-zag folding scheme.

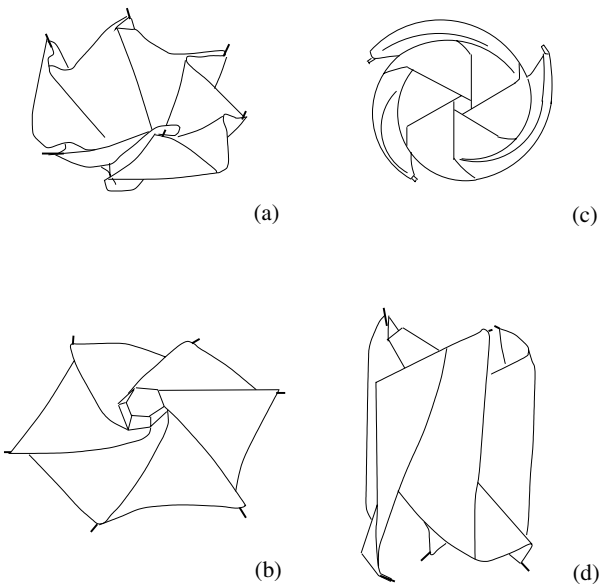

Figure 5.2: Wrapping scheme.

ring due to the light reflecting on the shiny Kapton surface, the membrane was painted black and the rib sleeves white.

5.1 Zig-Zag Folding

In the zig-zag folding technique each rib is folded in a radial plane by forming localised up and down folds. The sequence of folding has to be controlled very carefully, to avoid damaging the membrane. Two folds were introduced in each rib, a positive fold (up) near the hub and a negative fold (down) about half way along.

First, all the ribs were folded upwards and the membrane between each pair of ribs was pushed in the gap between them. Once the ribs had been folded, they were held against the perspex cylinder with two strings, one in the middle and one at the bottom of the ribs, see Figure. 5.3. The folded configuration at this stage is about 600 mm high, from the bottom to the tip of the ribs.

Figure 5.3: First step of zig-zag folding.

Then, the ribs were folded downwards —one by one— just above the position of the top string and masking tape was used to hold the tips of the folded ribs against the bottom of the hub. As the folding proceeded, the membrane was pulled out and wrapped around the folded ribs. Before folding the last rib, the top string was cut off and removed. Finally, an elastic band was placed in the middle of the package formed by the folded ribs and membrane, before removing the bottom string and the strips of masking tape.

Figure 5.4 shows the packaged configuration of the demonstrator. It is about 300 mm high and its diameter is about the same as the hub.

Figure 5.5 shows selected frames from the deployment sequence. Note that the time delay is 24 ms for the first 14 frames and 344 ms for the last two.

In the first three frames, 0-48 ms, the elastic band that holds the package is cut by hand to trigger the deployment; there was no interference between the

Figure 5.4: Zig-zag packaged configuration.

model and the scissors cutting the band. The initial deployment phase proceeded smoothly. Frames 72-96 ms show the upward folds opening out while the downward folds begin to open up after 120 ms. Frames 144-216 ms show the upward folds opening up much more quickly than the downwards folds. After frame 240 ms, all the upward folds have disappeared, and at this point the motion of the model slows down considerably. The remainder of the deployment sequence involves the slow motion of the downward folds. Finally, the model stopped in a partially folded configuration; clearly, this deployment test was unsuccessful.

A similar behaviour had been already observed by Seffen, You and Pellegrino (1997). This behaviour is typical of deployment tests with the concave side of the reflector facing up. Seffen at al. found that if the reflector faces down (gravity-assisted deployment) it deploys into the correct configuration.

5.2 Wrapping

In the wrapping technique, the ribs are supposed to be bent and twisted near the hub, in order to form a compact transition region, and then smoothly bent around the hub. They should be bent alternatively above and below their connections to the hub, in order to form a series of hill and valley folds in the membrane. In fact, the ribs of the demonstrator are rather short in comparison with the hub diameter and hence it was not possible to reach the end of the transition region. It was found that this folding technique is more difficult to implement since it is difficult to hold the bent and twisted ribs in their correct positions while other ribs have yet to be completely folded.

First, each rib was folded upwards towards the perspex cylinder. Unlike the zig-zag folding, the membrane between the ribs was pulled out. At this point, all the ribs should be twisted around the hub until they are all compactly packaged, but friction between the membrane and the cylinder was too high. Hence, three

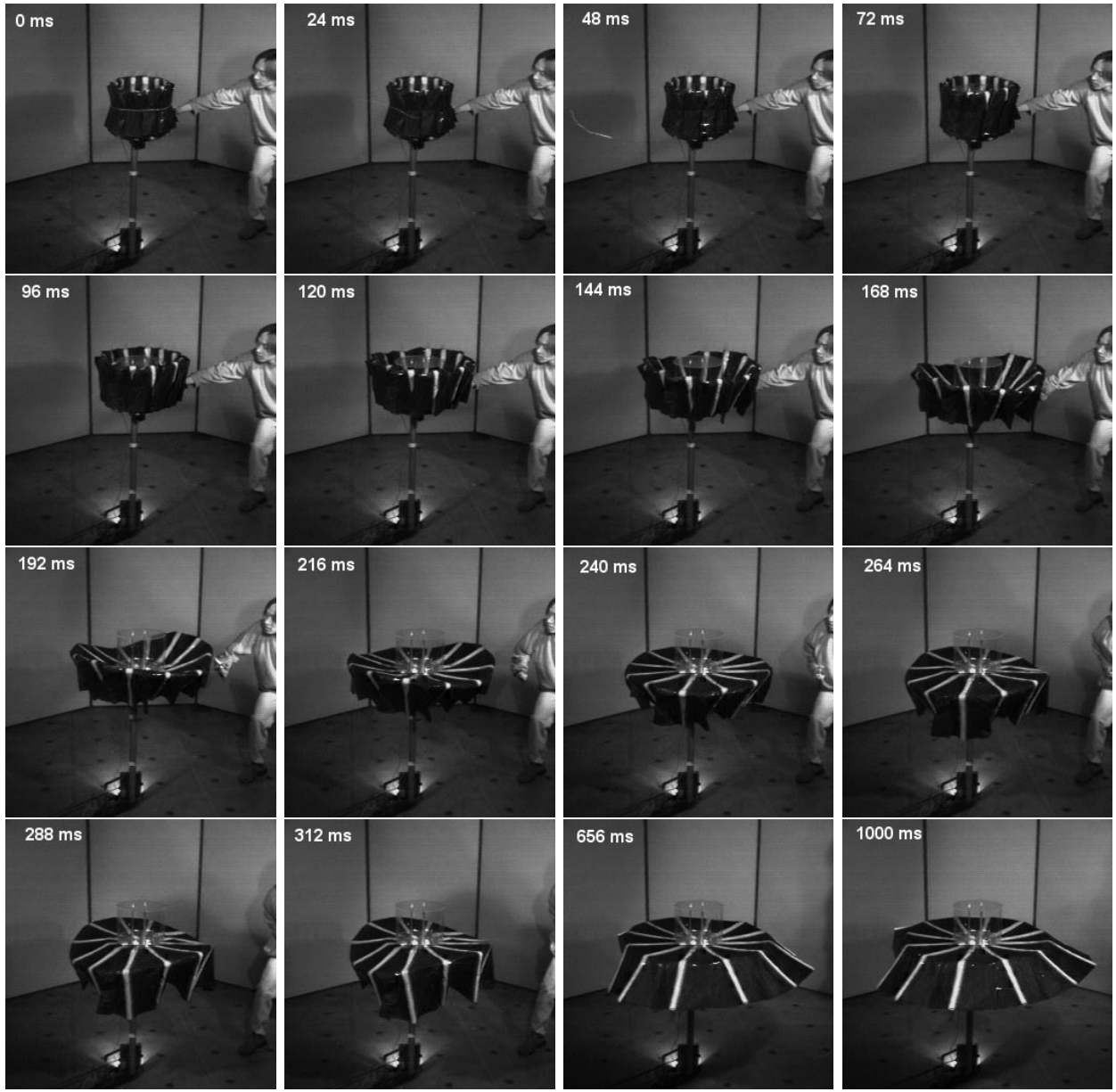

Figure 5.5: Deployment sequence, from top-left to bottom-right, of CRTS demonstrator packaged by zig-zag technique.

people were required to carry out the packaging, two holding the folded ribs while the third person went around the package, gradually bending and twisting one rib at a time towards its final configuration. When the packaged configuration had been finally achieved, an elastic band was used to hold it in position.

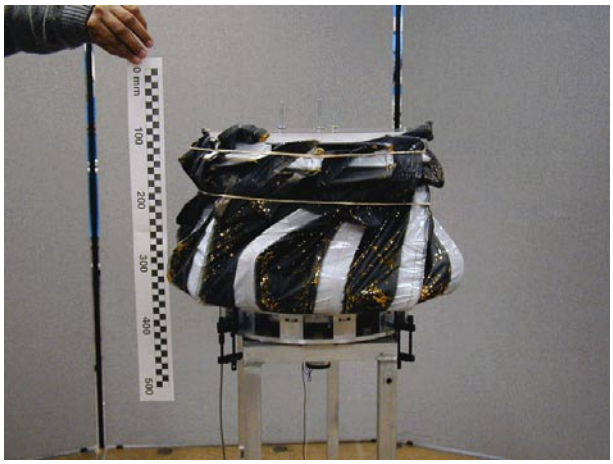

Figure 5.6: Demonstrator packaged by wrapping.

Figure 5.6 shows the final, packaged configuration. It can be seen that the ribs were not packaged very tightly, especially at the bottom. The height of the package is about 300 mm, about the same as with the zig-zag folding, but its diameter at the bottom is about 450 mm, as the ribs come out about 75 mm on each side. This was the best that could be achieved; it was found that the perspex cylinder does not support the bent and twisted ribs very well, and three of the ribs were found damaged at the end of the deployment test.[1]

Figure 5.7 shows selected frames from the deployment sequence. The time delay for the first 12 frames is 100 ms and 134 ms for the last four. In the first 400 ms of the deployment, the ribs unwrap, leaving a single fold in each rib, near the hub. Then, frames 500-1334 ms, the ribs deploy as cantilever beams connected by hinges to the hub. After 1334 ms all the folds have disappeared and the ribs have reached their fully deployed configuration. The remaining frames show a slow oscillation of the structure. In this case, deployment was completed successfully, but the deployment of the twelve ribs was less well coupled than previously observed by Seffen et al. (1997). This was probably due to the damage mentioned above.

This test confirmed a conclusion already reached by Seffen, You and Pellegrino (1997), that in the wrapping packaging scheme the membrane provides a useful coupling between the motion of the ribs. The correct deployed configuration

[1]However, note that several of the ribs used in the deployment tests had been damaged during a preliminary test, and were re-shaped by plastic deformation. It is likely that the three ribs found damaged at the end of deployment test described above had a lower yield stress, due to this repair.

is always reached, regardless of the orientation of the reflector with respect to gravity.

5.3 Folding Machine

Figure 5.8 shows a proposed folding machine that would help package a reflector with the wrapping technique. For clarity only one rib is shown.

The machine consists of a ring that holds the folds at the roots of the ribs, thus preventing them from being bent too tightly. A threaded rod is placed at the centre of the hub and is connected to a cylinder with a threaded hole in the middle. After folding all the ribs vertically upwards, their tips are temporary connected to the cylinder by threads. Then, the cylinder is turned slowly, thus twisting and bending the ribs at the same time. During this process, the membrane is pulled out and gradually wrapped together with the ribs. When the ribs are completely wrapped around the cylinder, the temporary connections between them and the cylinder are removed.

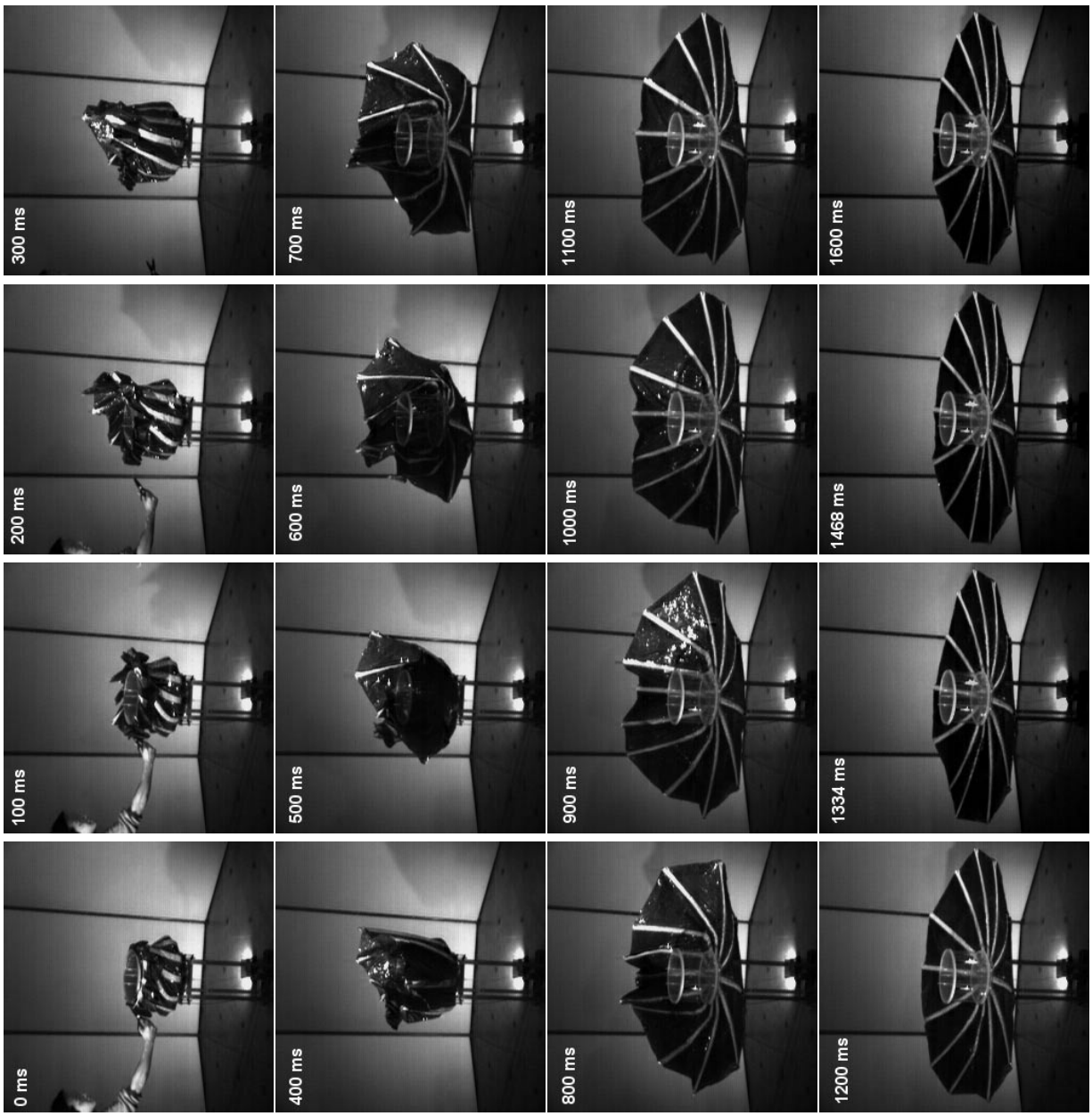

Figure 5.7: Deployment sequence of CRTS demonstrator packaged by wrapping technique.

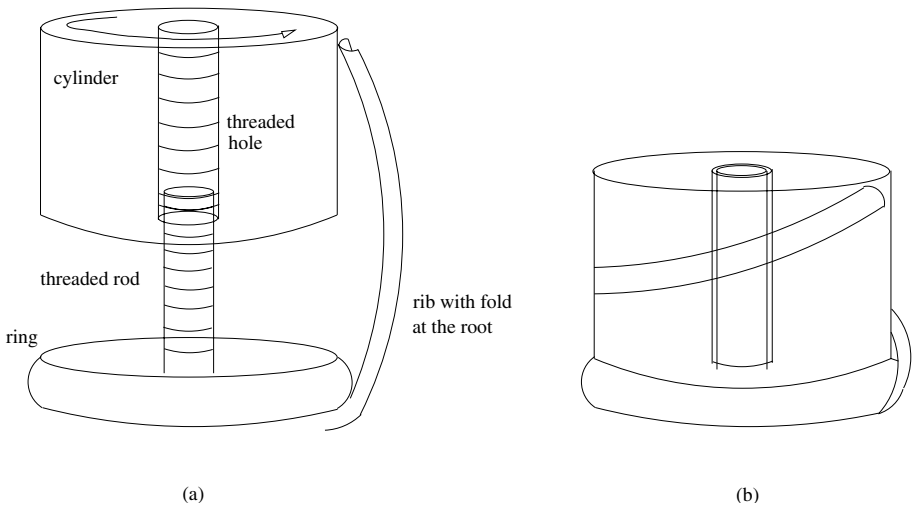

Figure 5.8: Proposed wrapping mechanism (a) start; (b) finish.

Chapter 6

Shape Measurement

After prestressing the reflector, its shape was measured with a 3D measurement system consisting of three Zeiss Eth2 electronic theodolites, connected to a personal computer (Kwan and You 1993). This system has an accuracy of ±0.1 mm.

6.1 Prestressing

The expansion of the hub and prestressing of the membrane surface are controlled by a steel cable wrapped around a set of pulleys inside the hub, see Section 2.2. This cable is terminated against the central disk and the pulley-1 holder, near rib 1; see Fig. 2.1 and 2.2. The cable termination at the pulley holder is shown in Fig. 6.1. During the expansion of the hub, the tension in the cable is monitored, so that the motor can be stopped when it reaches the value corresponding to the desired stress distribution.

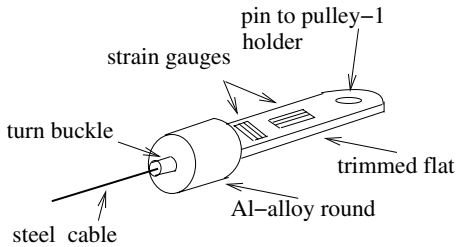

Figure 6.1: Cable termination.

The readings from the strain gauges were calibrated by hanging dead weights under the cable. Figure 6.2 shows a plot of the readings from the strain gauge metre against the cable force.

The cable tension required to equilibrate the rib loads listed in Table 3.5 is 7.2 N; this value corresponds to the prestress values in Table 1.1. Due to friction in the bearings and the soft springs attached to the back of each rib holder, the cable force needs to be increased by about 0.5 N. This value was obtained by direct measurement of the force required to expand the hub after disconnecting

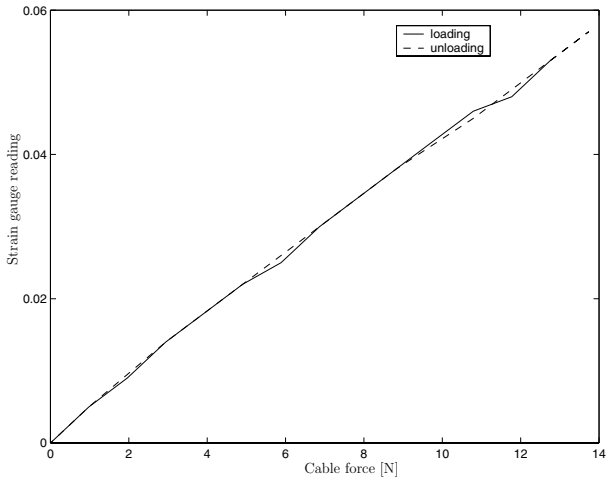

Figure 6.2: Cable force against strain gauge reading.

the ribs and membrane. Therefore, the required cable force is about 7.7 N, which corresponds to a strain gauge reading of 0.029.

6.2 Membrane Error

After prestressing the membrane it was observed that in a region about 100 mm wide around the hub several gores appear to be practically unstressed. Clearly, the cutting pattern was not sufficiently accurate in this region. This is because the accuracy required to achieve a hoop force per unit length of 40 N/m, which corresponds to a strain of

$$\frac{\sigma}{E} = \frac{40 \times 10^{-3}/0.1}{11.9 \times 10^{3}} = 33.6 \times 10^{-6} \tag{6.1}$$

The average distance between the edges of a gore in a 100 mm wide region near the hub is around 100 mm. Hence, the elastic extension of the membrane is about 4×10^{-3} mm which, of course, is not practically achievable.

A way of improving the prestress distribution in this area may be to remove the rib sleeves near the hub, in order to balance the hoop stress around the whole region, instead of gore-by-gore.

6.3 Shape Measurement

It was decided to measure 21 target points on each gore, uniformly distributed on the surface, plus 7 target points along each rib for further verification. This means that 252+84=336 target points were measured for the whole surface, corresponding to an average density of one measurement for a surface area of 6420 mm^2. Figure 6.3 shows the layout of the target points on a gore.

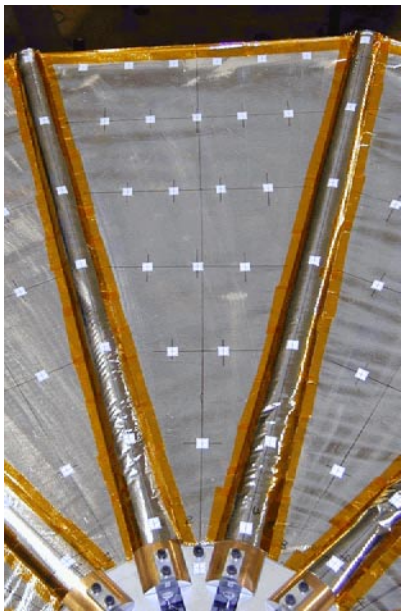

Figure 6.3: Layout of target points on a gore.

In the 3D measurement system the theodolites are labelled 1, 2 and 3 in an anti-clockwise sense, and provide the measured coordinates in a reference system defined such that the origin is at the centre of Theodolite 1, the Z-axis is vertical, and Theodolite 2 lies in the X-Z plane. The measured coordinates of the 252 points on the surface are listed in Appendix B.

After measuring all the points on the surface, the corresponding *rms* error was computed. Appendix A of Lai, You and Pellegrino (1997) gives the following expression for the *rms* error in the axial direction of a reflector whose surface, of area S, is defined by n uniformly distributed points, i.e. each node is associated with an area $s = S/n$

$$\delta Z = \sqrt{\frac{s \sum (\hat{Z}_i - Z_i)^2}{S}} \tag{6.2}$$

However, Fig. 6.3 shows that the target points were not uniformly distributed. In this case, Eq. 6.2 is modified by introducing different node areas s_i

$$\delta Z = \sqrt{\frac{\sum s_i (\hat{Z}_i - Z_i)^2}{S}} \tag{6.3}$$

The values of s_i were determined by dividing up each gore into a series of quadrangles whose areas were obtained from the finite element mesh used for form-finding.

Assuming the best-fit paraboloid to have an equation of the type

$$z = a(x^2 + y^2) + b \tag{6.4}$$

the best-fit coefficients a, b were computed using the experimentally measured points and a set of points lying on the theoretical surface, as close as possible to the measured points. Table 6.1 compares the best-fit coefficients that were obtained thus, as well as the corresponding *rms* error.

Note that the experimental *rms* error is 11% *lower* than expected, which is a surprising result because, of course, the physical model of the demonstrator cannot be more accurate than its idealised, i.e. "perfect" model. The distribution of the target points was first suspected, however a calculation of the *rms* error of a surface with uniformly distributed target points found the corresponding error to be 2.22 mm, i.e. practically unchanged. Hence, it seems unlikely that the discrepancy is due to the distribution of the target points on the surface. Since the discrepancy between experimental and predicted *rms* error is close to the accuracy of our measurement system, it was concluded that the two errors should be treated as practically coinciding.

	rms error [mm]	a	b
"Reference" surface	2.29	0.2784	0.0015
Shape measurement	2.0±0.1	0.2920	0.0000

Table 6.1: Error of predicted ("reference") and measured surfaces.

In order to further investigate the shape measurements, the measured coordinates of the points lying on the ribs were compared with the expected rib profiles, defined as the coordinates of the points of the reference surface, plus an increase in the Z-coordinate to allow for the depth of the rib. These plots are shown in Figure 6.4. Overall, the measured rib profiles match the analytical predictions very well. The largest deviation is around 4 mm.

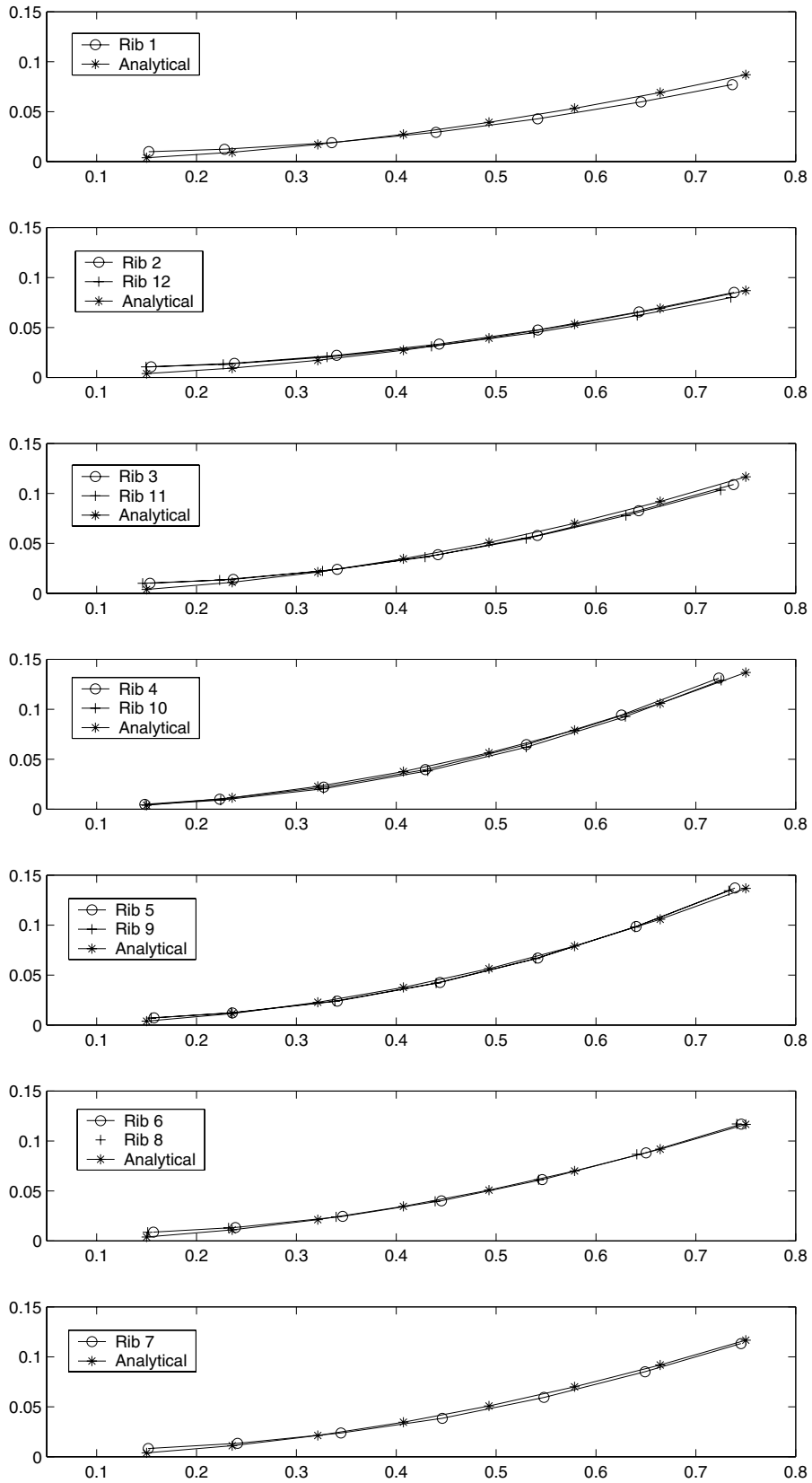

Figure 6.4: Predicted and measured rib profiles.

Chapter 7

Discussion and Conclusions

A complete design of a 1.5 m diameter offset CRTS reflector with focal length of 0.9 m was developed and implemented as a complete structural demonstrator, which was then tested. The layout of the reflector was based on the *circular configuration* proposed by Lai and Pellegrino (1999), which is such that the projection of the reflective surface onto the local tangent plane at the centre of the reflector approximates to a circle. With this layout, the projections of all the ribs of the reflector onto the tangent plane have the same length and the projections of the membrane gores are also identical. Therefore, an almost uniform state of prestress can be applied to the membrane without any out-of-plane loading on the ribs.

It is normally argued that to avoid the formation of wrinkles thin membranes need to be subjected to biaxial states of prestress, but an alternative approach was followed. Based on recent research by Wong (2000), which has shown that large wrinkles form only when either the membrane stretches or the boundary supports are non-smooth, the present design aimed for a distribution of prestress almost purely in the hoop direction. This approach has a number of advantages, as follows: (i) the reflector surface can be made from flat, in-plane stiff gores; (ii) the accuracy of the reflector can be easily predicted, as its shape coincides with the *reference surface* introduced by Lai and Pellegrino (1999); (iii) the calculation of the cutting patterns for the gores and the analysis of the elastic deformation of the ribs can be done quite accurately by considering simple two-dimensional models.

A hub mechanism design was developed, in which each rib is mounted on a linear bearing and is pulled outwards by a single steel cable that applies a prestressing force. The ratios between the rib forces, related to the number of ribs, diameter, offset and focal length of the reflector, are controlled by varying the diameter of the pulleys supporting this cable. The whole system is driven by a single electric motor.

This design has worked very well, but the present hub mechanism has a mass of $\approx$ 6 kg and contains a large number of moving parts. Clearly, a different, although kinematically equivalent design will be needed for use in space. An obvious change would be to mount the ribs on springs perpendicular to the plane

of the hub, thus removing all the linear guides. The idea of using a single cable to apply the prestressing forces to the base of each rib has also worked well. In future, the possibility of using a Nitinol wire —replacing both the steel cable and the electric motor, gears, and disk— is worth considering.

A general approach to the design of the curved ribs was presented. It takes into account the maximum bending moment in each rib and the yield limit when the ribs are folded during packaging. A rational approach to the design of the rib moulds was presented, taking into account the shape distortion of curved CuBe strips during heat treatment.

A procedure for accurately cutting the pieces of Kevlar-reinforced Kapton foil, bonding them along the edges to form the complete membrane of the reflector, attaching the Kevlar edge cord and the rib sleeves was developed. Of course, this is a key stage in the practical realisation of CRTS reflectors and great care was taken in describing the procedure that was followed, so that future developments can benefit from the present work.

Packaging techniques for CRTS reflectors were first investigated by You and Pellegrino (1994) who proposed two different schemes, zig-zag folding and wrapping. Of these two schemes, it was found that only wrapping works well for C-section ribs. The problem with zig-zag folding —confirmed by the present study— is that the downwards folds away from the hub are bi-stable, i.e. they can be in equilibrium in a half-deployed configuration. On the other hand, it was confirmed that if the membrane and ribs are wrapped around the hub, they then deploy very reliably. The deployment time of the 1.5 m demonstrator was about 1 s. Packaging the demonstrator was found to be far from straightforward, also due to its over-designed ribs, however it is believed that a folding machine could simplify this process considerably.

The surface accuracy of the demonstrator was carefully measured and its *rms* error was found to be 2.0 mm, slightly *lower* than the predicted value of 2.3 mm.

In conclusion, both the design methodology and the fabrication procedure were successfully validated.

7.1 Recommendations for further work

Based on the above discussion and points raised earlier in the report, the following recommendations for further work are made. The following list is in order of significance, i.e. the most important first.

- Move ribs under the reflective surface. This will require considerable changes to the design presented in this report; it is thought that a feasible approach would be to remove the rib sleeves, but instead connect the seam between adjacent gores directly to the upper edge of the ribs by means of “membrane webs.”

- Design and make a folding machine, to wrap the reflector.

- Modify the hub design to reduce the number of moving contacts. Explore the possibility of replacing the electric motor and steel cable with a Nitinol wire.
- More accurate measurement of surface accuracy, by increasing the number of target points.

Acknowledgments

Advice and encouragement from the ESA Project Manager, Mr W.J. Rits are gratefully acknowledged. The Kevlar-reinforced Kapton foil for the demonstrator was provided by Oerlikon-Contraves. Thanks are due to our colleagues Messrs. R.J. Denston, D. Green, P.J. Knott and A. Ross for technical support.

Bibliography

Bernasconi, M.C. and Rits, W.J. (1990). Inflatable, Space-Rigidized Support Structures for Large Spaceborne Optical Interferometer Systems. *Acta Astronautica*, **22**, 145-153.

Kukathasan, S. and Pellegrino, S. (2001). *Vibration of Prestressed Membrane Reflectors*. Department of Engineering, University of Cambridge, CUED/D-STRUCT/TR194.

Kwan, A.S.K. and You, Z. (1993). *User guide to Theo3, and industrial measurement system using three Zeiss ETh2 theodolites*. Department of Engineering, University of Cambridge Report CUED/D-STRUCT/TR142.

Lai, C.Y., You, Z. and Pellegrino, S. (1997). *Shape and stress analysis of symmetric CRTS reflectors* (Revised in 2001). Department of Engineering, University of Cambridge Report CUED/D-STRUCT/TR170.

Lai, C.Y. and Pellegrino, S. (1999). *Shape and stress analysis of offset CRTS reflectors* (Revised in 2001). Department of Engineering, University of Cambridge Report CUED/D-STRUCT/TR177.

Rits, W. J. (1996). A multipurpose deployable membrane reflector. *Esa Bulletin 88*, pp. 66-71.

Seffen, K. A. and Pellegrino, S. (1997). *Deployment of a rigid panel by tape-springs*. Department of Engineering, University of Cambridge Report CUED/D-STRUCT/TR168.

Seffen, K. A., You, Z. and Pellegrino, S. (1997). *Folding and deployment of curved tape springs*. Department of Engineering, University of Cambridge Report CUED/D-STRUCT/TR171.

Wong, Y. W. (2000). *Analysis of wrinkle patterns in prestressed membrane structures*. M.Phil. Dissertation, University of Cambridge, Department of Engineering.

You, Z. and Pellegrino, S. (1994). *Study of the folding and deployment aspects of a Collapsible Rib Tensioned Surface (CRTS) Antenna reflector.* Department of Engineering, University of Cambridge Report CUED/D-STRUCT/TR144.

Appendix A

Manufacturing Drawings

This appendix contains the drawings of the main components that were manufactured in the Workshops of the Engineering Department.

Appendix B

Measured Coordinates

The measured coordinates of the target points are listed. In each gore, the targets are measured starting from the point nearest to the hub and then, by rows left to right, towards the outer edge of the gore.

Target point	(X, Y, Z)[m]		
Gore 1			
1	1.8890	2.4455	-1.3109
2	1.9120	2.5462	-1.3030
3	1.9536	2.5270	-1.3025
4	1.9301	2.6463	-1.2915
5	1.9734	2.6253	-1.2908
6	2.0167	2.6067	-1.2897
7	1.9487	2.7469	-1.2769
8	1.9939	2.7257	-1.2758
9	2.0383	2.7056	-1.2746
10	2.0834	2.6854	-1.2734
11	1.9656	2.8486	-1.2594
12	2.0105	2.8270	-1.2582
13	2.0555	2.8062	-1.2570
14	2.1008	2.7849	-1.2561
15	2.1465	2.7636	-1.2547
16	1.9738	2.9307	-1.2440
17	2.0190	2.9081	-1.2435
18	2.0637	2.8871	-1.2424
19	2.1100	2.8665	-1.2404
20	2.1553	2.8453	-1.2385
21	2.2007	2.8233	-1.2365
Gore 2			
22	1.9776	2.3681	-1.3089
23	2.0441	2.4470	-1.2994
24	2.0706	2.4085	-1.2981
25	2.1121	2.5251	-1.2851
26	2.1394	2.4845	-1.2835
27	2.1645	2.4457	-1.2820
28	2.1787	2.5995	-1.2684
29	2.2051	2.5596	-1.2662
30	2.2332	2.5206	-1.2636
31	2.2608	2.4803	-1.2611
32	2.2431	2.6785	-1.2484
33	2.2713	2.6379	-1.2455
34	2.3001	2.5965	-1.2422
35	2.3274	2.5561	-1.2392
36	2.3559	2.5150	-1.2358
37	2.2932	2.7475	-1.2303
38	2.3222	2.7047	-1.2272
39	2.3505	2.6633	-1.2240
40	2.3780	2.6232	-1.2208
41	2.4072	2.5819	-1.2169
42	2.4359	2.5413	-1.2128

Table B.1: Coordinates of target points.

Target point	(X, Y, Z)[m]		
Gore 3			
43	2.0171	2.2579	-1.3069
44	2.1151	2.2894	-1.2942
45	2.1174	2.2434	-1.2944
46	2.2104	2.3256	-1.2765
47	2.2136	2.2756	-1.2757
48	2.2171	2.2301	-1.2748
49	2.3043	2.3576	-1.2545
50	2.3089	2.3074	-1.2525
51	2.3135	2.2587	-1.2503
52	2.3178	2.2105	-1.2483
53	2.4005	2.3897	-1.2273
54	2.4029	2.3412	-1.2252
55	2.4063	2.2929	-1.2227
56	2.4099	2.2428	-1.2199
57	2.4134	2.1940	-1.2172
58	2.4763	2.4296	-1.2035
59	2.4798	2.3797	-1.2000
60	2.4836	2.3297	-1.1961
61	2.4878	2.2795	-1.1936
62	2.4917	2.2301	-1.1901
63	2.4953	2.1802	-1.1849
Gore 4			
64	1.9941	2.1457	-1.3088
65	2.0931	2.1223	-1.2947
66	2.0732	2.0817	-1.2949
67	2.1939	2.1026	-1.2738
68	2.1724	2.0601	-1.2742
69	2.1519	2.0185	-1.2745
70	2.2927	2.0872	-1.2470
71	2.2713	2.0427	-1.2471
72	2.2508	1.9981	-1.2470
73	2.2304	1.9538	-1.2469
74	2.3865	2.0683	-1.2140
75	2.3656	2.0230	-1.2139
76	2.3447	1.9768	-1.2138
77	2.3252	1.9335	-1.2136
78	2.3056	1.8881	-1.2134
79	2.4748	2.0600	-1.1783
80	2.4530	2.0151	-1.1796
81	2.4331	1.9694	-1.1810
82	2.4117	1.9242	-1.1825
83	2.3905	1.8787	-1.1830
84	2.3695	1.8324	-1.1824

Table B.2: Coordinates of target points.

Target point	(X, Y, Z)[m]		
Gore 5			
85	1.9163	2.0532	-1.3092
86	1.9941	1.9872	-1.2959
87	1.9568	1.9617	-1.2969
88	2.0724	1.9198	-1.2757
89	2.0323	1.8917	-1.2772
90	1.9938	1.8636	-1.2783
91	2.1489	1.8543	-1.2498
92	2.1074	1.8256	-1.2518
93	2.0672	1.7970	-1.2535
94	2.0273	1.7673	-1.2551
95	2.2193	1.7898	-1.2182
96	2.1784	1.7622	-1.2209
97	2.1385	1.7322	-1.2229
98	2.1000	1.7044	-1.2259
99	2.0602	1.6741	-1.2283
100	2.2917	1.7398	-1.1842
101	2.2513	1.7107	-1.1891
102	2.2108	1.6819	-1.1929
103	2.1697	1.6533	-1.1964
104	2.1290	1.6244	-1.1993
105	2.0875	1.5948	-1.2019
Gore 6			
106	1.8066	2.0179	-1.3108
107	1.8391	1.9194	-1.2992
108	1.7936	1.9157	-1.3001
109	1.8719	1.8225	-1.2821
110	1.8237	1.8191	-1.2832
111	1.7762	1.8162	-1.2844
112	1.9059	1.7278	-1.2601
113	1.8559	1.7244	-1.2612
114	1.8068	1.7196	-1.2620
115	1.7577	1.7151	-1.2629
116	1.9354	1.6339	-1.2332
117	1.8867	1.6301	-1.2346
118	1.8385	1.6249	-1.2355
119	1.7880	1.6208	-1.2370
120	1.7394	1.6162	-1.2379
121	1.9733	1.5534	-1.2070
122	1.9248	1.5496	-1.2080
123	1.8740	1.5454	-1.2090
124	1.8240	1.5418	-1.2100
125	1.7741	1.5379	-1.2112
126	1.7246	1.5328	-1.2122

Table B.3: Coordinates of target points.

Target point	(X, Y, Z)[m]		
Gore 7			
127	1.6916	2.0384	-1.3120
128	1.6704	1.9381	-1.3013
129	1.6286	1.9576	-1.3020
130	1.6515	1.8378	-1.2857
131	1.6091	1.8583	-1.2862
132	1.5657	1.8791	-1.2867
133	1.6328	1.7368	-1.2642
134	1.5884	1.7576	-1.2648
135	1.5440	1.7787	-1.2653
136	1.4994	1.7991	-1.2654
137	1.6109	1.6391	-1.2387
138	1.5664	1.6608	-1.2393
139	1.5225	1.6819	-1.2400
140	1.4770	1.7039	-1.2403
141	1.4330	1.7244	-1.2404
142	1.6049	1.5530	-1.2145
143	1.5601	1.5743	-1.2150
144	1.5147	1.5964	-1.2156
145	1.4689	1.6174	-1.2157
146	1.4237	1.6381	-1.2159
147	1.3784	1.6608	-1.2163
Gore 8			
148	1.6032	2.1184	-1.3141
149	1.5351	2.0403	-1.3032
150	1.5102	2.0783	-1.3038
151	1.4695	1.9618	-1.2875
152	1.4424	2.0023	-1.2871
153	1.4154	2.0418	-1.2869
154	1.4048	1.8840	-1.2655
155	1.3757	1.9256	-1.2650
156	1.3468	1.9660	-1.2641
157	1.3193	2.0067	-1.2631
158	1.3382	1.8086	-1.2398
159	1.3111	1.8511	-1.2390
160	1.2829	1.8922	-1.2377
161	1.2556	1.9321	-1.2364
162	1.2284	1.9728	-1.2350
163	1.2841	1.7389	-1.2144
164	1.2559	1.7793	-1.2127
165	1.2279	1.8209	-1.2112
166	1.1991	1.8625	-1.2088
167	1.1712	1.9039	-1.2065
168	1.1429	1.9452	-1.2036

Table B.4: Coordinates of target points.

Target point	(X, Y, Z)[m]		
Gore 9			
169	1.5637	2.2228	-1.3149
170	1.4663	2.1940	-1.3039
171	1.4628	2.2397	-1.3041
172	1.3697	2.1605	-1.2860
173	1.3654	2.2094	-1.2862
174	1.3623	2.2563	-1.2867
175	1.2757	2.1243	-1.2621
176	1.2714	2.1746	-1.2624
177	1.2672	2.2235	-1.2627
178	1.2626	2.2731	-1.2632
179	1.1803	2.0935	11.2308
180	1.1776	2.1423	11.2322
181	1.1740	2.1916	11.2335
182	1.1701	2.2397	11.2345
183	1.1661	2.2891	11.2350
184	1.1014	2.0566	11.2020
185	1.0973	2.1068	11.2033
186	1.0929	2.1562	11.2042
187	1.0895	2.2061	-1.2051
188	1.0860	2.2561	-1.2053
189	1.0814	2.3066	-1.2049
Gore 10			
190	1.5861	2.3395	-1.3147
191	1.4852	2.3626	-1.3052
192	1.5051	2.4027	-1.3057
193	1.3851	2.3832	-1.2890
194	1.4058	2.4260	-1.2905
195	1.4270	2.4670	-1.2919
196	1.2869	2.4011	-1.2671
197	1.3071	2.4448	-1.2689
198	1.3273	2.4883	-1.2709
199	1.3488	2.5320	-1.2730
200	1.1902	2.4192	-1.2394
201	1.2105	2.4635	-1.2424
202	1.2313	2.5082	-1.2454
203	1.2513	2.5520	-1.2481
204	1.2722	2.5960	-1.2499
205	1.1040	2.4288	-1.2055
206	1.1251	2.4732	-1.2102
207	1.1461	2.5187	-1.2154
208	1.1669	2.5648	-1.2205
209	1.1883	2.6101	-1.2247
210	1.2086	2.6554	-1.2273

Table B.5: Coordinates of target points.

Target point	(X, Y, Z)[m]		
Gore 11			
211	1.6609	2.4285	-1.3145
212	1.5869	2.4989	-1.3066
213	1.6246	2.5243	-1.3068
214	1.5078	2.5642	-1.2938
215	1.5475	2.5914	-1.2946
216	1.5871	2.6191	-1.2954
217	1.4305	2.6302	-1.2759
218	1.4709	2.6591	-1.2774
219	1.5118	2.6866	-1.2793
220	1.5511	2.7146	-1.2809
221	1.3519	2.6967	-1.2545
222	1.3941	2.7254	-1.2570
223	1.4343	2.7527	-1.2593
224	1.4762	2.7808	-1.2618
225	1.5169	2.8095	-1.2639
226	1.2850	2.7448	-1.2321
227	1.3257	2.7742	-1.2377
228	1.3675	2.8021	-1.2409
229	1.4072	2.8311	-1.2438
230	1.4488	2.8599	-1.2459
Gore 12			
231	1.4916	2.8880	-1.2471
232	1.7714	2.4672	-1.3123
233	1.7424	2.5648	-1.3053
234	1.7873	2.5685	-1.3042
235	1.7077	2.6622	-1.2951
236	1.7545	2.6660	-1.2944
237	1.8026	2.6701	-1.2936
238	1.6743	2.7585	-1.2812
239	1.7239	2.7631	-1.2808
240	1.7729	2.7674	-1.2803
241	1.8217	2.7719	-1.2797
242	1.6390	2.8540	-1.2637
243	1.6898	2.8582	-1.2631
244	1.7374	2.8626	-1.2625
245	1.7887	2.8658	-1.2623
246	1.8384	2.8697	-1.2622
247	1.6033	2.9301	-1.2489
248	1.6528	2.9344	-1.2501
249	1.7030	2.9383	-1.2501
250	1.7530	2.9421	-1.2497
251	1.8032	2.9458	-1.2488
252	1.8537	2.9499	-1.2467

Table B.6: Coordinates of target points.